Effects of rheological models of blood on the flow through an idealised stenosed artery

Milanović, Matko

University of Zagreb
Faculty of Mechanical Engineering and Naval Architecture

MASTER'S THESIS

Matko Milanović

Zagreb, 2022.

University of Zagreb
Faculty of Mechanical Engineering and Naval Architecture

MASTER'S THESIS

Effects of rheological models of blood on the flow through an idealised stenosed artery

Mentor:
Prof. Željko Tuković, PhD
Prof. Peter De Jaeger, PhD

Student:
Matko Milanović

Zagreb, 2022.

I would like to thank my mentor prof. Željko Tuković, PhD on provided support, advice and time dedicated during this thesis. I would also like to thank my co-mentor prof. Peter De Jaeger, PhD. and AZ Delta hospital in Belgium for supporting this thesis. I would also like to acknowledge assistant Philipp Milović, MSc for all the provided materials and unselfish help during this thesis. Most importantly, I would like to thank my family, friends and my girlfriend for their unconditional support over the course of my studies.

Statement | Izjava

I hereby declare that I have made this thesis independently using the knowledge acquired during my studies and the cited references.

Izjavljujem da sam ovaj rad radio samostalno koristeći znanja stečena tijekom studija i navedenu literaturu.

Zagreb, July 2022 Matko Milanović

SVEUČILIŠTE U ZAGREBU
FAKULTET STROJARSTVA I BRODOGRADNJE
Središnje povjerenstvo za završne i diplomske ispite
Povjerenstvo za diplomske ispite studija strojarstva za smjerove:
Procesno-energetski, konstrukcijski, inženjersko modeliranje i računalne simulacije i brodostrojarski

Sveučilište u Zagrebu Fakultet strojarstva i brodogradnje	
Datum	Prilog
Klasa: **602 - 04 / 22 - 6 / 1**	
Ur.broj: **15 - 1703 - 22 -**	

DIPLOMSKI ZADATAK

Student: **Matko Milanović** JMBAG: 0035209591

Naslov rada na hrvatskom jeziku: **Utjecaj reoloških modela krvi na strujanje kroz idealiziranu stenozu arterije**

Naslov rada na engleskom jeziku: **Effects of rheological models of blood on the flow through an idealised stenosed artery**

Opis zadatka:

Computational fluid dynamics methods have been frequently utilised for hemodynamics studies of the circulatory system, especially in recent years. Of special interest is the flow through stenosed arteries, i.e., arteries with a sudden reduction in cross sectional area, which usually results from plaque build-up. When modelling the flow through stenosed arteries it is often assumed that blood behaves like a Newtonian fluid, with the stress-strain relationship being linear, even though this is not entirely accurate. It has been proven that the viscosity of blood decreases as the shear rate increases, a process often referred to as "shear-thinning". Certain viscoelastic properties of blood have also been observed, primarily the existence of a yield stress, below which flow does not occur. Given that the choice of rheological model can significantly impact the flow state, it is necessary to assess the effects of different models such that an adequate hemodynamic analysis of stenosed arteries can be performed.
The aim of this thesis is to conduct a numerical analysis of flow through an idealised stenosed artery using different rheological models and assess the impact of model choice on the flow characteristics at different Reynolds numbers. Assuming a laminar, isothermal flow of an incompressible fluid through a rigid-wall tube with varying cross-sectional area, it is necessary to compare the effects of three rheological models of blood:

- Newtonian
- generalised Newtonian
- viscoelastic

The effects of model choice are to be analysed for both steady and oscillatory flow. The obtained results should be compared to those available in the literature wherever possible.
It is necessary to list the references used in this work, and to acknowledge any help or support possibly received during the course of this study.

Zadatak zadan:	Datum predaje rada:	**Predviđeni datumi obrane:**
5. svibnja 2022.	7. srpnja 2022.	18. – 22. srpnja 2022.

Zadatak zadao:

Prof.dr.sc. Željko Tuković

Izv.prof.dr.sc. Peter De Jaeger
AZ Delta, Belgium

DocuSigned by:
Peter De Jaeger
F007A5C59B4D4BE...

Predsjednik Povjerenstva:

Prof. dr. sc. Tanja Jurčević Lulić

Contents

List of Figures

List of Tables

List of Symbols

Sažetak

Koronarna bolest srca je česta i ozbiljna bolest koja nastaje kao posljedica nakupljanja plaka na koronarnim arterijama. Uzrokuje smanjenje površine poprečnog presjeka arterije što otežava protok krvi.
U ovom radu napravljena je numerička analiza strujanja krvi kroz idealiziranu stenotičnu arteriju. Analiziran je utjecaj reološkog modela krvi na strujne karakteristike. Krv je modelirana kao Newtonovski, generalizirani Newtonovski te viskoelastični fluid. Za modeliranje generaliziranog Newtonovskog fluida korišten je Carreau-Yasuda model, a za modeliranje viskoelastičnog fluida korišten je pojednostavljeni Phan-Thien–Tanner (sPTT) model. Proučavano je stacionarno i nestacionarno strujanje za tri različite geometrije stenoze pri vrijednostima Reynoldsovog broja 50 i 200. Rezultati pokazuju da Carreau-Yasuda model predviđa najmanji granični sloj i znatno manje magnitude brzina u osi arterije u usporedbi s ostalim modelima. Razlike između modela su primjetnije kada je stenoza veća te pri većim brzinama strujanja. Rezultati ovog rada su uspoređeni s rezultatima analize provedene u radu Chauchan & Sasmal [7].

Ključne riječi: Stenoza, hemodinamika, računalna dinamika fluida, reološki modeli, generalizirani Newtonovski, viskoelastičnost

Summary

Coronary artery disease is a common and serious disease which is a consequence of plaque build-up in the coronary arteries. As a result, the artery cross-sectional area is reduced which restricts the blood flow.
In this study, a numerical analysis of the blood flow through an idealised stenosed artery is presented. The effects of rheological models of blood on the flow characteristics is studied. Blood is modeled as a Newtonian, a generalized Newtonian and a viscoelastic fluid. For generalized Newtonian fluid modelling, the Carreau-Yasuda model is used. For viscoelastic fluid modelling, the simplified Phan-Thien-Tanner (sPTT) model is used. Flow is studied as steady and transient for three different stenosis geometries at Reynolds number values of 50 and 200. Results show that the Carreau-Yasuda model predicts the smallest boundary layer size and significantly lesser velocity magnitudes at the artery axis in comparison to the other models. The differences between model predictions are more noticeable when the stenosis is more severe and at higher velocities. Results of this study are compared to the results from the study of Chauchan & Sasmal [7].

Keywords: Stenosis, hemodynamics, computational fluid dynamics, rheological models, generalized Newtonian, viscoelasticity

1 Introduction

Coronary artery disease (CAD) is one of the leading causes of death globally. Arteries can exhibit local diameter reduction (stenosis) due to build up of plaque on the inner walls. As a result, blood and oxygen supply through the body is reduced. It is usually the plaque rupture that causes the acute and lethal cases of CAD. Identifying the plaque which is at the most risk of rupture is difficult even with today's technology. CFD, or Computational Fluid Dynamics, is a technology that has greatly benefited research in many areas, including medicine. It provides us with the insight into fluid behaviour without the need to perform physical experiments. Performing physical experiments in medicine can be expensive, lengthy and even dangerous to the patient's well-being. CFD use in medicine has accelerated the development of new treatment and diagnostic methods. Hemodynamics is a study of blood flow through the cardiovascular system. In recent years, hemodynamic studies have been increasingly using CFD as a research tool.

1.1. Cardiovascular system

The heart, blood vessels and blood make up the cardiovascular system. Its missions are, amongst many others, to transport nutrients and remove waste products from the body. The heart is the organ that can be considered as a blood pump. It relaxes and contracts periodically. These contractions allow for the blood to be supplied where it is needed throughout the body. The blood vessels are channels through which the blood flows. Blood is the liquid that carries nutrients and oxygen. The length of all blood

Figure 1.1: Cardiovascular system [1]

vessels combined is estimated to be around 100 000 kilometers. [2] That is enough to encircle the entire Earth more than twice. Blood velocity and pressure vary greatly in relation to the blood vessel dimension. For example, velocity in arteries reaches up to 45 cm/s while in capillaries it is approximately 0.3 mm/s. The pressure varies from 120 mmHg and 80 mmHg due to pulsating heart behaviour. In capillaries, it is between 35 and 17 mmHg [3].

1.2. Heart

The heart is the primary organ of the cardiovascular system. It is made up of cardiac muscle tissue, or myocardium, which is found nowhere else in the body. It is approximately the size of a fist and positioned in the front left side of the chest. Four chambers make up the heart as shown in Figure 1.2, the left and right atrium and the left and right ventricle. Blood flows through the blood vessels due to the pressure

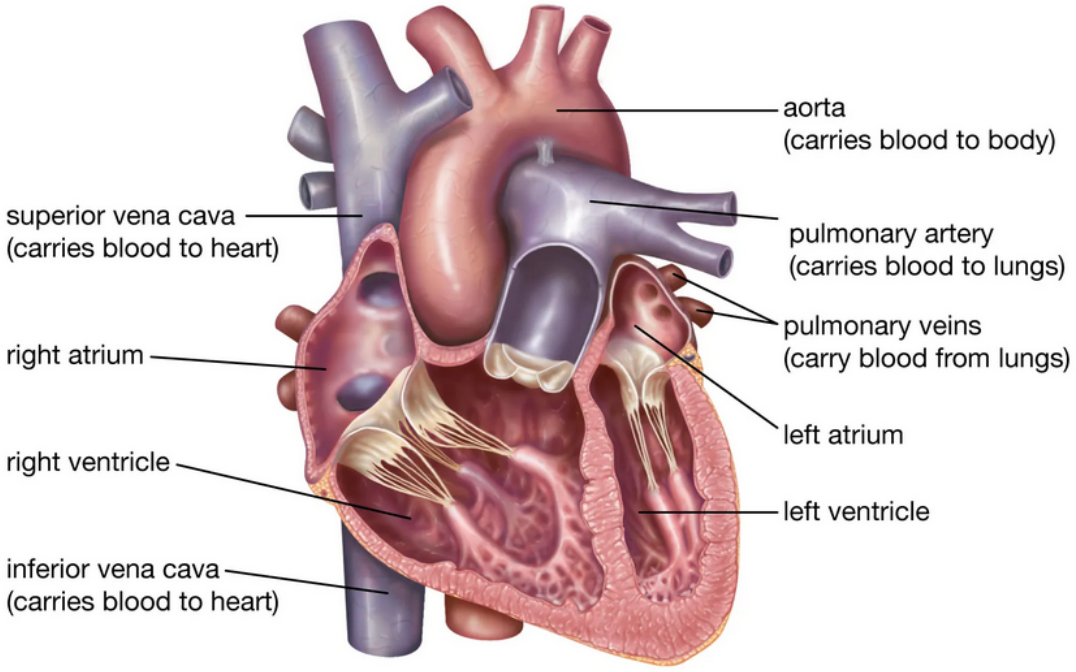

Figure 1.2: Heart structure [4]

difference in ventricular outlet and atrial inlet. Blood from the rest of the body enters the heart on the right side. That blood is low in oxygen and is pumped through the lungs to receive oxygen. After the lungs, oxygenated blood returns to the left side of the heart and is then further distributed to the body through the largest artery called aorta.

Besides pumping blood throughout the body, it also controls the heart rate and maintains blood pressure. Between the chambers on each side there are heart valves such as tricuspid and mitral valve. They open and close periodically due to heart contraction and allow blood flow in one direction. This is what is called a heart beat. A typical heart beat for an adult is 60 to 100 times per minute. It can increase depending on various physical or psychological factors. Blood pressure shows how much force the blood flow exerts on the walls of the blood vessels. It is measured in *mmHg* and usually presented as 2 numbers. First number being the systolic pressure which shows the pressure during heart contraction and second number being the diastolic pressure showing the pressure in the heart's relaxation period. Healthy blood pressure is between 90/60 mmHg and 120/80 mmHg.

1.3. Blood vessels

Blood vessels are responsible for blood distribution in the body. They can be divided into three categories:

- Arteries
- Veins
- Capillaries

Arteries transport oxygenated blood away from the heart. They are characterized by thick walls and a layer of muscular tissue which helps move the blood. The aorta is the largest artery in the body, measuring up to 48 cm in length. [5]
Veins bring the deoxygenated blood back to the heart. They are usually wider in diameter than arteries, but have thinner walls. There is no muscular tissue inside the walls of veins.
Capillaries are the smallest blood vessels and can measure as little as 5μm in diameter [6]. They are a connection between arteries and veins. They are present in all bodily tissue and carry both oxygenated and deoxygenated blood.

1.4. Blood

Blood is a red fluid circulating through blood vessels, supplying the body with nutrients and oxygen while removing waste. It is mostly liquid, and made up of plasma and blood cells. It consists of approximately 55% plasma and 45% erythrocytes, leukocytes and thrombocytes. Numerous proteins and nutrients are suspended in the plasma. Approximately 5 liters of blood is pumped by the heart each minute during the rest phase. During physical activity, the blood flow can increase to 20 liters per minute. Its average density is 1060 $\frac{kg}{m^3}$ [7].

1.5. Coronary artery disease and stenosis

When the flow of blood through the vessels is obstructed, it presents a significant risk to health and well-being. Coronary artery disease is the build-up of plaque in

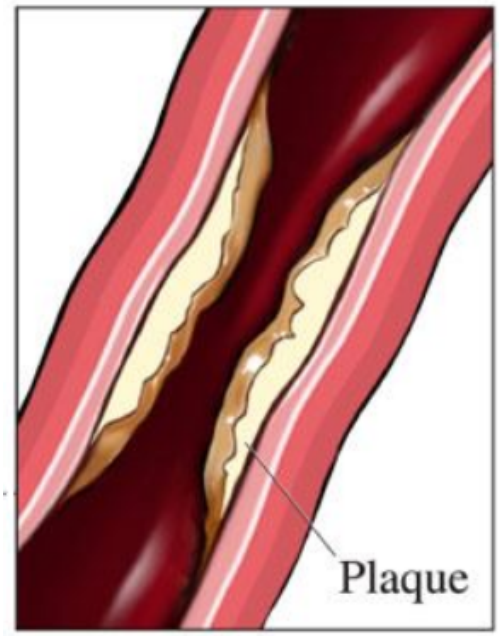

Figure 1.3: Coronary artery stenosis [8]

the coronary arteries. Plaque consists of fatty substances, cholesterol, cellular waste product, calcium and fibrin. [9] Plaques develop over time and grow in size. The reduction of the cross-sectional area of the artery is called stenosis (see Figure 1.3).

According to literature [10], most of the ruptures occur when 45-50% of the cross-sectional area of the artery is blocked. If this reduction happens gradually over time, the vascular network can adapt by creating additional arterioles. Another possible compensation is the widening of the pressure-regulating arterioles which results in increased blood velocity in the stenosis upstream. However, this results in additional load to the plaque.

1.6. Blood rheology

Blood rheology is the study of blood deformation and its flow. Viscosity of blood is dependent on many factors such as red blood cells, plasma, blood pressure [11] etc. Numerous studies have been carried out treating blood as a Newtonian fluid such as water, meaning that the viscosity is treated as a constant, independent of shear stress. Plasma itself, which is the most of the blood, behaves as a Newtonian fluid, while blood

as a whole behaves as a non-Newtonian fluid. Non-Newtonian fluids are characterized by varying viscosity dependent on the shear rate. Shear rate is the rate at which fluid layers move past each other. It is illustrated in Figure 1.4 which shows the imaginary layers of the fluid with a dy height at two different points in time, $t = 0$ and $t = dt$. The bottom layer is attached to the stationary surface. Therefore, the velocity of the bottom layer is $U = 0$. Upper layers are moving with gradually increasing velocities. Due to viscosity of the fluid, each layer is affected by the neighbouring layers. Slower layers try to slow down the faster layers and vice versa. After time dt, the top layer covers the distance of dx. Shear strain is the ratio of the displacement dx and the height dy. It is also a tangent of an angle denoted with $d\theta$ in Figure 1.4. Further in this study, that angle will be denoted with $d\gamma$. For infinitesimally small values of $d\gamma$, the shear strain is defined as [12]:

$$\tan d\gamma \approx d\gamma = \frac{dx}{dy} \tag{1.1}$$

The rate of change of the angle $d\gamma$ is known as the shear rate. It is often denoted with $\dot{\gamma}$ and is equal to the velocity gradient in y direction:

$$\dot{\gamma} = \frac{d\gamma}{dt} = \frac{dU}{dy} \tag{1.2}$$

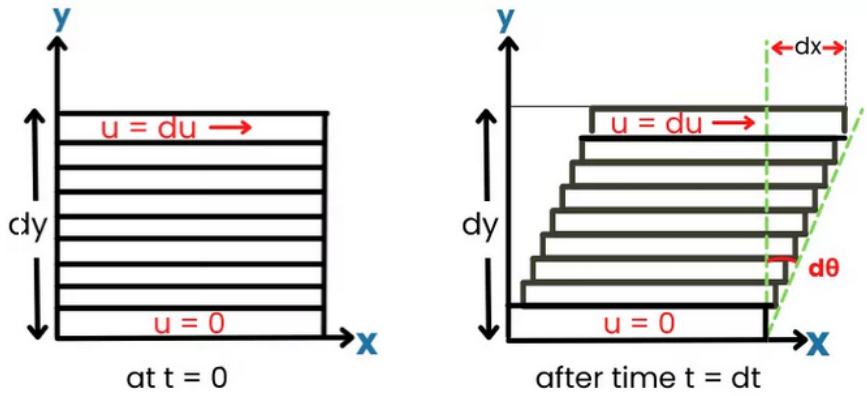

Figure 1.4: Shear rate [12]

To further illustrate this phenomenon, shear stress is defined by the Newtonian law of viscosity as:

$$\tau = \mu \cdot \frac{d\gamma}{dt} \tag{1.3}$$

where τ is the shear stress and μ is dynamic viscosity.

If the fluid is Newtonian, dynamic viscosity is constant and the relation between shear rate and shear stress is linear, as shown in Figure 1.5. Non-Newtonian fluids can exhibit either increase or decrease in viscosity in relation to shear rate progression. If the viscosity is increased, the fluid is called *shear-thickening* fluid. If the viscosity is decreased, the fluid is called *shear-thinning* fluid. Blood falls into this category. In addition to non-Newtonian properties, blood also displays elastic properties and those properties vary due to red blood cells concentration. Primarily, the existence of a limiting shear stress value before which no flow can occur. At higher concentrations, the elastic properties are greater. When concentration exceeds 20%, the elastic properties increase with red blood cells to the power of three, while effective viscosity increases exponentially [13]. Red blood cells are elastic and can deform under shear stress. Therefore, they release elastic energy to the flow. At higher velocity gradients however, the elastic properties are decreased. The blood flow is largely dominated by its viscous properties rather than

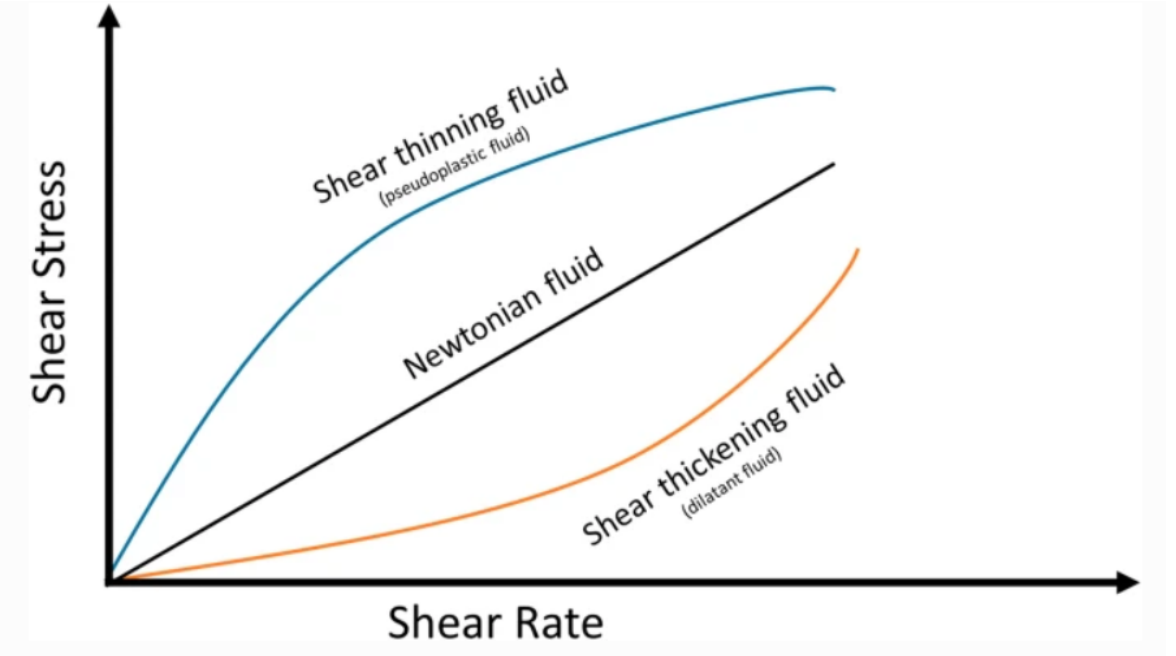

Figure 1.5: Shear rate dependency on shear stress for Newtonian and non-Newtonian fluids [14]

its elastic properties, especially at large velocity gradients. However, red blood cells can

build up in certain regions of the flow based on local flow conditions. In those regions, elastic properties can have greater influence on the flow characteristics than viscous properties.

1.7. Aim of this thesis

In this study, a numerical analysis of the blood flow through an idealised stenosed artery is conducted. The flow is assumed to be laminar, isothermal and incompressible. The aim of this study is primarily to assess the effects of rheological model choice on the characteristics of blood flow. The comparison is done for three different rheological models:

- Newtonian
- Generalized Newtonian
- Viscoelastic

The height and the width of the stenosis are varied. Three different stenosis shapes are used. The analysis is done for two values of Reynolds number, $Re = 50$ and $Re = 200$. The impact of varying stenosis shape and Reynolds number on the flow characteristics is also investigated. Furthermore, analysis is done for both steady and pulsatile flow. In total, 36 separate numerical simulations are done, 18 for steady and 18 for pulsatile flow. As a means of results validation, results of this study are compared to those presented in the study of Chauchan & Sasmal [7].

2 Fundamentals of Fluid Mechanics

Fluid mechanics is the study of liquid and gas behaviour in both static and dynamic circumstances. In fluid mechanics, fluids are considered as continuous matter. The continuum model allows for the material to keeps its physical properties even when the volume is reduced to virtually zero. As a result, fluids can be described in an idealized way where every particle takes up only one particular point in space.
Fluid dynamics, a branch of fluid mechanics, is the study of fluid in motion and its interaction with solids. It is governed by 5 main conservation principles:

- Conservation of mass
- Conservation of linear momentum
- Conservation of angular momentum
- Conservation of energy
- Second law of thermodynamics

Since it is assumed that the flow is isothermal and that there is no energy exchange between blood and the artery wall, the conservation of energy equation is not relevant in this study. Entropy is not present in other equations and can be solved separately. Therefore, and second law of thermodynamics is also not presented. By assuming that there is no torque present at the surface or inside the material volume, then the stress tensor $\tau_{ij} = \tau_{ji}$ is symmetric. If the symmetry of the stress tensor is assumed beforehand, then the conversation of angular momentum is already obeyed. Therefore, the conserva-

tion of angular momentum equation is also not shown. In this study, only conservation of mass and linear momentum are relevant, so only those two will be presented.

2.1. Material and Control Volume

All the governing equations stated above are initially written in terms of a material volume. A material volume is the volume closed by the imaginary boundary surface, consisting of the same particles at all times. It can change its shape and position, but never lose its particles. This makes material volumes unsuitable for fluid dynamics applications, since the interest is not in the tracking of certain particles, but in the consequences of fluid motion near a solid structure.
If another set of imaginary boundary surfaces is defined, but ones which allow for particle passage, a control volume is defined. A control volume is then an arbitrarily defined volume, enclosed by fixed boundary surfaces. To transform the governing equations into control volume terms, the Reynolds Transport Theorem (RTT) is used. The RTT states that the rate of change of a physical property in a material volume is equal to the rate of change of the property per unit of time for a control volume and the flux of the property through the control surface CS.

$$\frac{D}{Dt}\int\limits_{MV}\phi\cdot dV=\frac{d}{dt}\int\limits_{CV}\phi\cdot dV+\int\limits_{CS}\phi\cdot u_j\cdot n_j dS \tag{2.1}$$

$$\frac{D}{Dt}\int\limits_{MV}\phi\cdot dV=\frac{d}{dt}\int\limits_{CV}\phi\cdot dV+\int\limits_{CS}\phi\cdot (u_j-u_{j,s})\cdot n_j dS \tag{2.2}$$

where u_j is the material velocity vector,$u_{j,s}$ is the control surface velocity vector at the surface dS, n_j is the normal vector, MV is the material volume and CV is the control volume. Equations 2.1 and 2.2 are forms of RTT transformation for a stationary and moving control surface, where ϕ is the physical property.

2.2. Conservation of mass

The mass conservation principle states that the rate of mass change inside the material volume is equal to zero.

$$\frac{D}{Dt}\int\limits_{MV}\rho\cdot dV=0 \tag{2.3}$$

If RTT is applied to Equation 2.3, the mass conservation equation is transformed to control volume terms.

$$\frac{d}{dt}\int\limits_{CV} \rho \cdot dV + \int\limits_{CS} \rho \cdot u_j \cdot n_j \cdot dS = 0 \tag{2.4}$$

Equation 2.4 states that the rate of change of mass inside the control volume, plus the net mass flow through the control surface is equal to zero at all times.

2.3. Conservation of linear momentum

Conservation of linear momentum or Newton's second law states that the momentum of an isolated system is constant. In material volume terms, it can be said that the rate of momentum change of a material volume is equal to the sum of all forces exerted on a material volume.

$$\frac{D}{Dt}\int\limits_{MV} \rho \cdot u_i \cdot dV = \int\limits_{MV} \rho f_i \cdot dV + \int\limits_{MS} \sigma_i \cdot dV \tag{2.5}$$

Term f_i is the body force per unit mass vector, σ_i is the stress vector representing the surface forces per unit area and MS is the surface of the material volume. When RTT is applied, the conservation of linear momentum equation can be written in control volume terms.

$$\frac{d}{dt}\int\limits_{CV} \rho \cdot u_i \cdot dV + \int\limits_{CS} \rho \cdot u_i \cdot u_j \cdot n_j \cdot dS = \int\limits_{CV} \rho \cdot f_i \cdot dV + \int\limits_{CS} \sigma_i \cdot dS \tag{2.6}$$

Equation 2.6 states that the rate of linear momentum change in the control volume plus the net flow of linear momentum through the control surface is equal to the sum of body and surface forces exerted on the control volume.

2.4. Reynolds number

Reynolds number Re is one of the most important dimensionless parameters in fluid mechanics. It represents the ratio of inertial forces to viscous forces. Its value also provides information on flow behaviour, and it is the main criteria for laminar to turbulent flow transition (see Figure 2.1). Laminar flow occurs at low Reynolds numbers and is

characterized by orderly flow in which particles flow in layers and there is no overlapping of streamlines. Turbulent flow on the other hand is a highly disordered flow that occurs at high Reynolds number when inertial forces are dominant, Streamlines are irregular and mixing is intense.

$$Re = \frac{\rho U L}{\mu} = \frac{\text{inertia forces}}{\text{viscous forces}} \tag{2.7}$$

Equation 2.7 is the expression for Reynolds number calculation. U is the characteristic velocity, ρ is the fluid density, L is the characteristic length scale of flow and μ is the dynamic viscosity of the fluid. The critical Reynolds number is defined as a lower

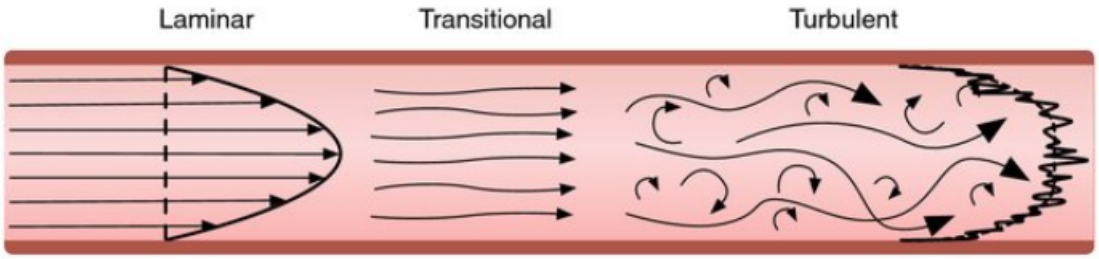

Figure 2.1: Laminar to Turbulent flow transition [15]

and an upper value. The values depend on many parameters. One of those parameters is the geometry in which or over which the fluid is flowing. For an internal pipe flow, the lower value of critical Reynolds number is 2300, while the upper value is 4000 or even more. This means that if the Reynolds number is lower than 2300, fully laminar flow is present. If the value is between 2300 and 4000, flow disturbances start to occur. When the value is greater than 4000, the flow is fully turbulent. The blood flow is usually laminar while flow disturbances can occur at branch points of larger arteries or in the ascending aorta. The appearance of disturbances is undesirable as they lead to increase in friction losses and the heart requires more energy to pump blood. [16] Since the artery is not a straight pipe with constant cross-sectional area and known surface roughness, the exact values of critical Reynolds number are unknown.

2.5. Modelling of blood flow

In this study, blood flow is investigated for Reynolds number values of 50 and 200 due to the possibility of results comparison with literature. The flow is assumed to be laminar, incompressible and isothermal. Density is constant at 1060 $\frac{kg}{m^3}$.
The effects of 3 rheological models on blood flow are investigated. The first model treats blood as a simple Newtonian fluid with constant dynamic viscosity of 0.0035 $Pa \cdot s$ as experiments tend to yield this value for shear rates greater than 200 s^{-1}.
The second model used is the Carreau-Yasuda model, which models blood as a non-Newtonian fluid. It is a commonly used empirical equation used to fit experimental data from non-Newtonian shear-thinning fluids.

$$\frac{\mu - \mu_\infty}{\mu_0 - \mu_\infty} = [1 + (k\dot{\gamma})^a]^{\frac{n-1}{a}} \tag{2.8}$$

where:

- μ_0 = viscosity at zero shear rate
- μ_∞ = viscosity at infinite shear rate
- k = characteristic time
- n = power law index
- a = parameter that decribes curvature in inital transition phase (see Figure 2.2)

Experimental data was taken from the study of Yeleswarapu et al. [17]. The data was fitted to Equation 2.8 and the resulting coefficients are shown in Table 2.1. The viscosity equation provides information on viscosity for a wide range of shear rates. The third model used is the simplified four modes Phan-Thein-Tanner model (sPTT). This model takes into account both the elasticity and the shear-thinning behaviour of blood when calculating shear stress. Viscoelasticity of blood is modelled in the same way as in

Table 2.1: Resulting coefficients of the Carreau-Yasuda model

μ_0	μ_∞	k	n	a
0.056	0.00345	1.902	0.22	1.25

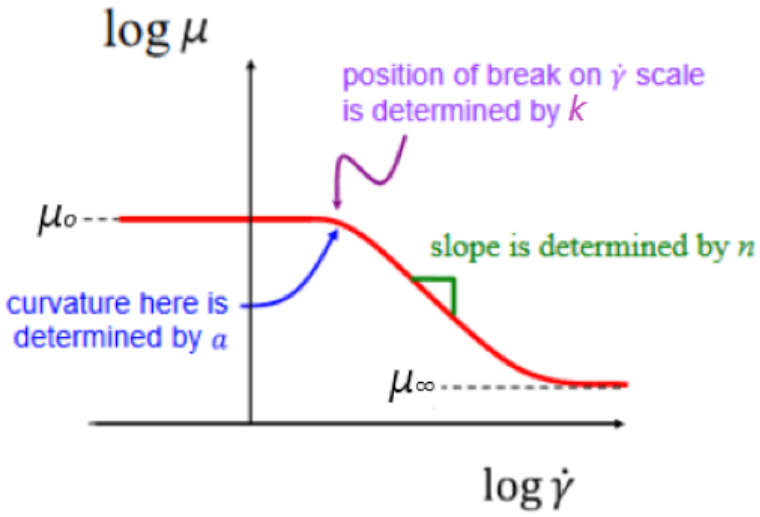

Figure 2.2: Viscosity dependency on shear rate for GNF [18]

Chauchan & Sasmal [7]. For better understanding of this model, the linear momentum equation can be written as:

$$\rho\left(\frac{\partial u_i}{\partial t}+u_j\frac{\partial u_i}{\partial x_j}\right)=-\frac{\partial p}{\partial x_i}+\frac{\partial \tau_{ij}}{\partial x_j} \tag{2.9}$$

where τ_{ij} is the shear stress tensor and it consists of two components:

$$\tau_{ij}=\tau_{ij}^{s}+\tau_{ij}^{p} \tag{2.10}$$

τ_{ij}^{s} is the solvent stress contribution and τ_{ij}^{p} is the viscoelastic component stress contribution. Furthermore, these components can be modelled by the following equations:

$$\tau_{ij}^{s}=2\mu_s D_{ij} \tag{2.11}$$

$$D_{ij}=\frac{1}{2}\left(\frac{\partial u_j}{\partial x_i}+\frac{\partial u_i}{\partial x_j}\right) \tag{2.12}$$

$$\tau_{ij}^{p}=\sum_{k=1}^{N}\tau_{ij}^{k} \tag{2.13}$$

$$f(\tau_{nn}^{k})+\lambda_k\overset{\nabla}{\tau}_{ij}^{k}-\alpha_k\frac{\lambda_k}{\mu_p^{k}}\left(\tau_{in}^{k}\cdot\tau_{nj}^{k}\right)=-2\mu_p^{k}D_{ij}^{k} \tag{2.14}$$

$$f(\tau_{nn}^k) = 1 + \frac{\lambda_k \epsilon_k \tau_{nn}^k}{\mu_p^k} \tag{2.15}$$

where:

- λ_k = relaxation time $[s]$
- μ_p^k = viscosity contribution to the zero-shear viscosity for k^{th} mode $[Pa \cdot s]$
- α_k = mobility factor (0 for sPTT model) $[-]$
- ϵ_k = extensibility coefficient $[-]$

In Equation 2.14, the $\overset{\nabla}{\tau}_{ij}^k$ term is the so called upper-convected derivative of the shear stress tensor of the k-th mode. It is defined by the following equation:

$$\overset{\nabla}{\tau}_{ij}^k = \frac{\partial \tau_{ij}^k}{\partial t} + u \cdot \nabla \tau_{ij}^k - (\nabla u)^T \cdot \tau_{ij}^k - \tau_{ij}^k \cdot \nabla u \tag{2.16}$$

where ∇ is the gradient and $(\nabla u)^T$ is the transpose matrix of the velocity gradient. The Equation 2.16 is a time derivative of the shear stress tensor immersed in a fluid with the velocity field u. [19] Values of the sPTT parameters are taken from Chauchan & Sasmal [7] and are shown in Table 2.2.

Table 2.2: multi-mode sPTT viscoelastic model parameters [7]

Mode (k)	μ_p^k	λ_k	ϵ_k
1	0.05	7	0.2
2	0.001	0.4	0.5
3	0.001	0.04	0.5
4	0.0016	0.006	0.5
5 (solvent)	0.0012	0	0

3 Computational Fluid Dynamics

Most of the fluid dynamics problems are defined by nonlinear partial differential equations which do not have a general analytical solution. With the technology advancement and increasing computational power available, it became possible to numerically solve the mathematical models of fluid flow. Computational Fluid Dynamics (CFD) began to develop. At the beginning of each simulation, a mathematical model is defined. The next step in pre-processing is the space discretization and as a result, a computational mesh is created. It is important for the mesh generation to be done correctly as the validity of the results can highly depend on mesh quality, especially for complex geometries. It is also important to take into account appropriate boundary conditions in the pre-processing phase. The next step is the equation discretization which is done using one of the following methods; Finite Element Method, Finite Volume Method or Finite Difference Method. In this thesis, the Finite Volume Method is used. It holds advantages over the Finite Difference Method, whose application is limited to simple geometries, such as rectangular and circular shapes. [20] The Finite Element Method is generally used for structural problems. The final step of the processing phase is the solution of discretized equations. Not all CFD softwares are suitable for all applications. Commercial softwares generally do not offer much flexibility when it comes to solver choice. Free, open source CFD software OpenFOAM offers a wide variety of solvers and for that reason it was used in this study. On the other hand, commercial softwares such as Fluent make up for the lack of flexibility in the simplicity of the work flow and user-friendliness. After the numerical solution is done, the results are analysed and visualized. Insight into forces, momentum, heat flux and so on is possible. This

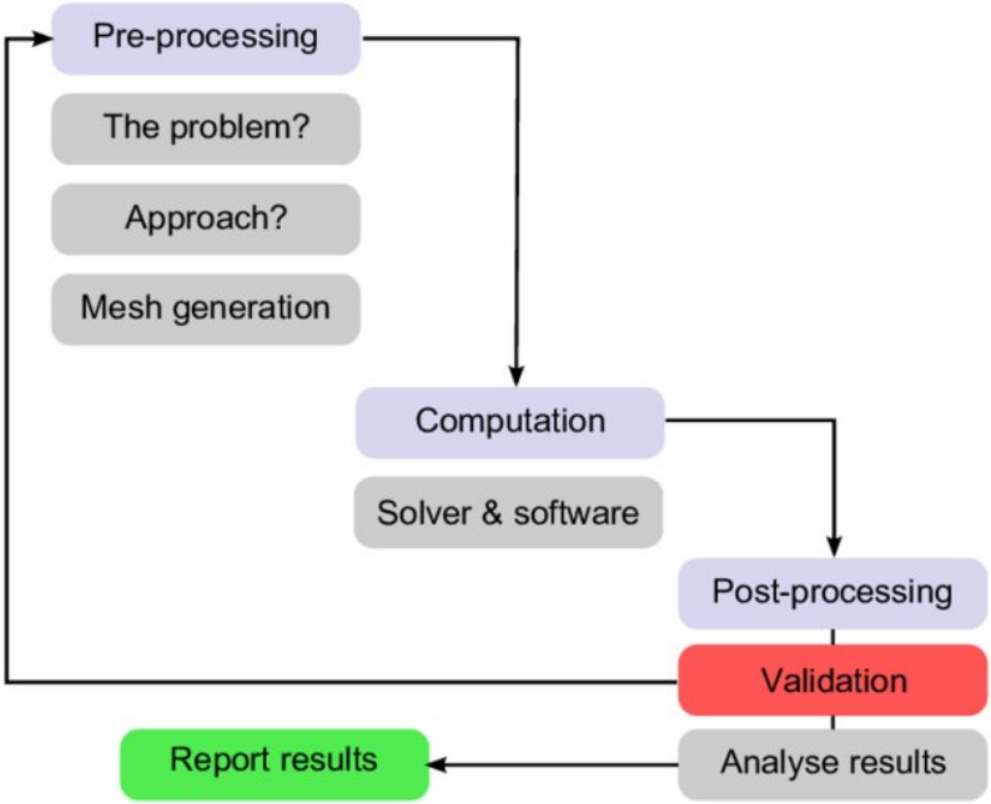

Figure 3.1: CFD simulation algorithm [21]

phase is called post-processing. In comparison to experimental studies, CFD has many advantages. It reduces the design time and gives the full picture of fluid flow. The number of physical prototypes can be reduced drastically. Furthermore, it is possible to simulate conditions which are not possible in an experimental environment. Generally, CFD analysis is faster and cheaper than the experimental. However, its limitations are in the existence of good mathematical models. For example, turbulent flow modelling can be a real issue. All in all, experimental studies and CFD are mutually beneficial. For complex issues, it is necessary to combine both approaches.

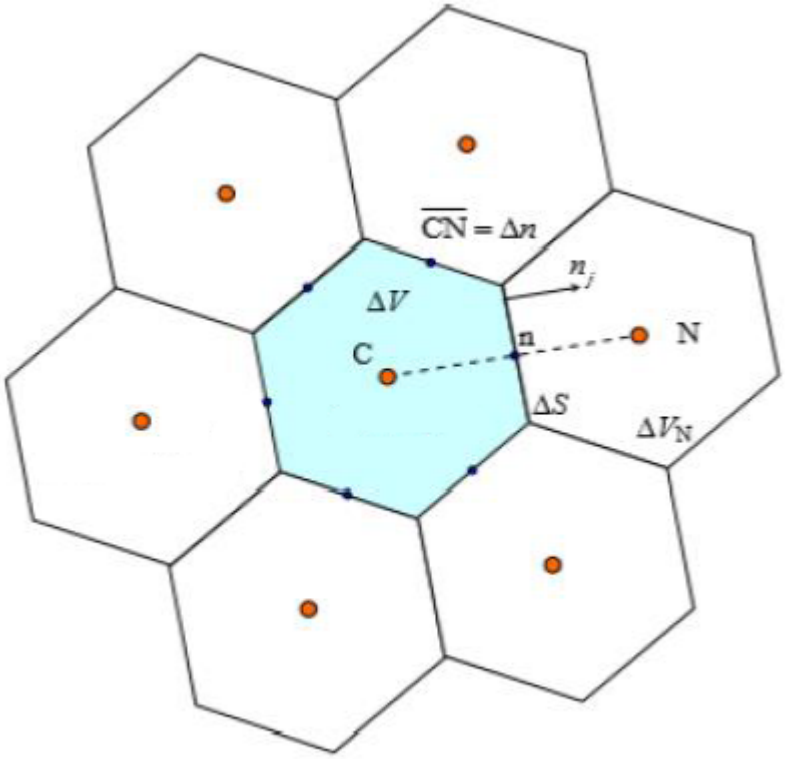

Figure 3.2: Finite Volume Method [20]

3.1. Finite Volume Method

Finite Volume Method (FVM) is the most commonly used method for equation discretization in fluid dynamics. As a result of discretization, a set of linear algebraic equations is obtained. That set of equations is then appropriate for iterative solvers. By space discretization, the space domain is divided into a number of finite volumes, each occupying a defined position without overlapping. FVM is suitable for fluid flow applications because it is fully conservative, meaning that the transported quantities are fully conserved, regardless of geometry mesh density. The basis of this method is the integration of conservative form of transport equations (3.1) over the finite volumes on geometry mesh. [20]

$$\frac{\partial(\rho\varphi)}{\partial t} + \frac{\partial(\rho u_j \varphi)}{\partial x_j} - \Gamma \frac{\partial^2 \varphi}{\partial x_j x_j} = \frac{\partial(\rho\varphi)}{\partial t} + \frac{\partial}{\partial x_j}\left(\rho u_j \varphi - \Gamma \frac{\partial \varphi}{\partial x_j}\right) = S_\varphi \qquad (3.1)$$

$\frac{\partial(\rho\varphi)}{\partial t}$ is the local change term, $\frac{\partial(\rho u_j\varphi)}{\partial x_j}$ is the convective term, $\Gamma\frac{\partial^2\varphi}{\partial x_j x_j}$ is the diffusive term, $\left(\rho u_j\varphi - \Gamma\frac{\partial\varphi}{\partial x_j}\right)$ is the flux vector and S_φ is the source term. When integrated over finite volume, Equation 3.1 becomes:

$$\frac{d}{dt}\int\limits_{\Delta V}\rho\varphi dV = -\int\limits_{\sum\Delta S}\left(\rho u_j\varphi - \Gamma\frac{\partial\varphi}{\partial x_j}dS\right)n_j + \int\limits_{\Delta V}S_\varphi dV \tag{3.2}$$

where the first term represents the rate of change of physical property φ inside the volume ΔV, the second term represents the convective and diffusive flux of φ through the boundary surfaces and the third term is the source term. The flux of φ is defined as positive when it is directed from the finite volume to surroundings and negative otherwise. Therefore, by definition, the amount of physical property is reduced due to the minus sign before the flux term. The volume and surface integral can be approximated by mean value theorem, with $\rho = const$:

$$\int\limits_{\Delta V}\varphi dV = \bar{\varphi}\Delta V \tag{3.3}$$

where $\bar{\varphi}$ is the mean value of the physical property φ in the finite volume. The rate of change of φ can be approximated as linear, with first-order Taylor polynomial around the center of the finite volume (point C in 3.1.):

$$\varphi(x_j) = \varphi_C + \frac{\partial\varphi}{\partial x_j}\Big|_C(x_j - x_j^C) \tag{3.4}$$

where x_j is a position vector of any point in the finite volume. Then, Equations 3.3 and 3.4 are combined:

$$\bar{\varphi}\Delta V = \int\limits_{\Delta V}\varphi dV = \varphi_C\Delta V + \frac{\partial\varphi}{\partial x_j}\Big[\int\limits_{\Delta V} -x_j^C\Delta V\Big] = \Big[\varphi_C + \frac{\partial\varphi}{\partial x_j}\Big|_C(x_j^T - x_j^C)\Big] \tag{3.5}$$

where x_j^T is the position vector at the center of gravity of the finite volume. If point C is the center of gravity of the final volume, then the right term on the right side of Equation 3.5 is equal to zero. Then the value of $\bar{\varphi} = \varphi_C$. Source term can be described in the same way.

$$\int\limits_{\Delta V}S_\varphi dV = S_C\Delta V \tag{3.6}$$

where S_C mean value of source term. Surface integrals in 3.2 are the convective and diffusive terms of φ flux through the surface. If those two vectors are added, they make

up for the total flux vector J_j. The flux of physical property is contributed only by the normal component of the flux vector $J_j n_j$ and it can be written as:

$$\Delta J_n = \left[\rho(\overline{u_n \varphi})_n - \Gamma \overline{\frac{\partial \varphi}{\partial n}}\Big|_n \right] \Delta S \tag{3.7}$$

where $(\overline{u_n \varphi})_n$ is the mean value of the product at the surface ΔS and can be approximated by the product of mean values. $\overline{\frac{\partial \varphi}{\partial n}}\Big|_n$ is the mean value of normal derivative of the field φ. Dimensionless coordinate $\tilde{n} = n/\Delta n$ can be introduced. Then the equation 3.7 is formed as:

$$\Delta J_n = (\rho \bar{u_n} \Delta S)_n \, \bar{\varphi_n} - \frac{\Gamma \Delta S}{\Delta n} \overline{\frac{\partial \varphi}{\partial \tilde{n}}}\Big|_n = F_n \varphi_n - D_n \frac{\partial \varphi}{\partial \tilde{n}}\Big|_n \tag{3.8}$$

where F_n is the convection intensity, and D_n is the diffusion intensity. A dimensionless parameter called local Peclet number can be defined. It carries information about which mechanism of transfer is dominant on a local scale.

$$Pe_L = \frac{F_n}{D_n} \tag{3.9}$$

As the volumes get smaller (Δn), diffusion gets more dominant over convection. If (Δn) becomes infinitesimally small, then the convection can be neglected entirely. Considering that in the numerical procedure, only the values of field φ at the finite volumes centers (points C and N) are calculated, it is necessary to approximate the value at the boundary surfaces of a finite volume (i.e. point n). This is called a numerical scheme. Approximation will be most precise if those values are defined in the center of gravity of surface ΔS. Using the equations 3.3, 3.6 and 3.8, equation 3.2 can be written as:

$$\rho \Delta V_c \frac{d\varphi_c}{dt} = -\sum_{nb=1}^{N_{nb}} \left(F_n \bar{\varphi_n} - D_n \overline{\frac{\partial \varphi}{\partial \tilde{n}}}\Big|_n \right)^{nb} + S_c \Delta V_c \tag{3.10}$$

where nb sum represents addition on all N_{nb} boundary surfaces of the finite volume. Using the numerical scheme, equation 3.8 is transformed to:

$$\Delta J_n = F_n \bar{\varphi_n} - D_n \overline{\frac{\partial \varphi}{\partial \tilde{n}}}\Big|_n = F_n \varphi_C + a_N (\varphi_C - \varphi_N) \tag{3.11}$$

where a_n coefficient is dependent on the choice of numerical scheme. If 3.11 is combined into 3.10, the transport equation is:

$$\rho \Delta V_C \frac{d\varphi_c}{dt} = -a_C \varphi_C + \sum_{nb=1}^{N_{nb}} [a_N \varphi_N]^{nb} + S_C \Delta V_C \tag{3.12}$$

and the central coefficient a_C is:

$$a_C = \sum_{nb=1}^{N_{nb}} [a_N]^{nb} \tag{3.13}$$

To obtain the linear algebraic equation, the source term is linearized as:

$$S_C \Delta V_C = a + b\varphi_C \tag{3.14}$$

Then the Equation 3.12 is implicitly integrated:

$$\rho \Delta V_C \frac{\varphi_C - \varphi_C^{old}}{\Delta t} = -\varphi_C \sum_{nb=1}^{N_{nb}} a_N^{nb} + \sum_{nb=1}^{N_{nb}} [a_N \varphi_N]^{nb} + a + b\varphi_C \tag{3.15}$$

$$\left(\frac{\rho \Delta V_C}{\Delta t} + \sum_{nb=1}^{N_{nb}} -b \right) \varphi_C = \sum_{nb=1}^{N_{nb}} [a_N^{nb} [a_N \varphi_N]^{nb} + a + \frac{\rho \Delta V_C}{\Delta t} \varphi_C^{old} \tag{3.16}$$

$$a_C \varphi_C = \sum_{nb=1}^{N_{nb}} [a_N^{nb} \varphi^{nb}] + b \tag{3.17}$$

Equation 3.17 is the linear algebraic equation for one finite volume. If the procedure is repeated for every finite volume, a set of linear algebraic equations is defined in which the unknown variables are values of φ. The number of equations is equal to the number of finite volumes. That set of equations can be written in matrix form:

$$[Aji][\varphi_i] = [bj] \tag{3.18}$$

where $[Aji]$ matrix contains a_C coefficients on the main diagonal and a_N^{nb} coefficients as well, $[\varphi_i]$ is the unknown vector and $[b_j]$ is a vector containing all known values. If the source term is a nonlinear function of φ then the numerical procedure will be iterative. All the equations presented in this chapter are taken from the work of Virag & Džijan [20].

4 Numerical setup

Numerical calculations are performed in an open-source CFD software called OpenFOAM. [22] A $v2012$ version of the software is used. [23] Some of its advantages over other CFD softwares are a more detailed insight in the computation, greater flexibility to modify the setup and the implementation of wide variety of solvers to suit specific needs. Both steady and transient simulations are solved using the PISO (Pressure Implicit with Splitting of Operator) algorithm and it consists of the following steps [24]:

1. Boundary conditions setup
2. Computation of an intermediate velocity field from the discretized momentum equation
3. Computation of the mass fluxes at the cells faces
4. Solve the pressure equation
5. Correction of mass fluxes at the cell faces
6. Velocity correction
7. Boundary condition update
8. Repeat from step 3. until converged
9. Increment time step and repeat from 1.

In the PISO algorithm, the operators are split into the predictor and corrector steps and the velocity and pressure fields are considered solved after the solutions of the corrector

steps converges. A maximum number of outer iterations is pre-determined in the setup at 1 for the PISO algorithm. Another important parameter for transient simulations is the Courant number and is defined as:

$$Co = \frac{U \cdot \Delta t}{\Delta x} \tag{4.1}$$

where U is the flow velocity, Δt is the time step and Δx is the the one dimensional mesh cell size. It represents a distance that a fluid particle covers in a single time step. If the $Co =$ number value is greater than one, the particle passes more than one cell in a time step and it means that the chosen time step is too large. The $Co =$ number value should be kept below one to prevent skipping of the cells. This is also known as the Courant-Friedrichs-Lewy (CFL) stability condition. In this study, the value of Courant number is kept at 1. Jasak et al. [25] developed a solver called *viscoelasticFluidFoam* which is used in this paper for viscoelastic simulations. In the study of Chauchan & Sasmal [7], a modified version of this solver was used. It efficiently and accurately predicts viscoelastic fluid behaviour even at high Weissenberg numbers. This dimensionless number is defined as:

$$Wi = \frac{\lambda_m u_{z,avg}}{R_0} \tag{4.2}$$

where λ_m is the mean relaxation time, $u_{z,avg}$ is the mean axial velocity and R_0 is the characteristic radius. Mean relaxation time λ_m is defined by:

$$\lambda_m = \frac{\sum_{k=1}^{N} \mu_p^k \lambda_k}{\sum_{k=1}^{N} \mu_p^k} \tag{4.3}$$

Higher values of Wi indicate greater elastic properties and this has been a problem for computational rheology for a long time. Linear sets of equations are solved with GAMG (Geometric Agglomerated Algebraic Multigrid Solver) solver. Gradients are discretized with *cellLimited leastSquares* method. All divergence terms are discretized with *Gauss GamaV* scheme. Residual tolerances are set at 10^{-7} for pressure values and 10^{-8} for velocity and wall shear stress values. Since the PISO solver is used, under-relaxation is not necessary. All schemes are of the second order of accuracy. Second order schemes are more difficult to converge, but are more accurate than the first order schemes.

Table 4.1: Stenosis geometry configuration [7]

Configuration	a	b	Area reduction
M0	$0,5 \cdot R_0$	R_0	75%
M1	$0,333 \cdot R_0$	$4R_0$	56%
M2	$0,667 \cdot R_0$	$4R_0$	89%

4.1. Geometry

The artery is taken as pipe with constant radius ($R_0 = 1$), apart from the stenosis. Both inlet and outlet length is taken as $50 \cdot R$ in order for the flow to be fully develop before reaching the stenosis section. In reality, artery walls are elastic but they are considered rigid in this study. The shape of the stenosis is described with the following relation:

$$\frac{r}{R_0} = 1 - \frac{a}{2R_0}\left[1 + cos\frac{\pi z}{b}\right] \; ; -b \leq z \leq b \tag{4.4}$$

where:

- a = stenosis height
- b = stenosis half-length
- R_0 = unobstructed pipe radius
- z = axial coordinate
- r = radial coordinate

In the same way as it is done in Chauchan&Sasmal [7], three different types of stenosis are studied (see Table 4.1.).

The simulations are done for an axisymmetric slice of the artery, a wedge (see Figure 4.1). The wedge boundary condition is set at the front and back sides of the domain. In order for this to work, the front and back patches must be separated by a single layer of cells (see Figure 4.2) . It is used to define an axisymmetric geometry such as a cylinder or an artery in this case. The centerline (z-axis) is the symmetry axis. Both geometry and the flow are assumed to be axisymmetric along the z-axis. Therefore, all tracked values such as velocity or pressure are constant at a certain radius for all angles.

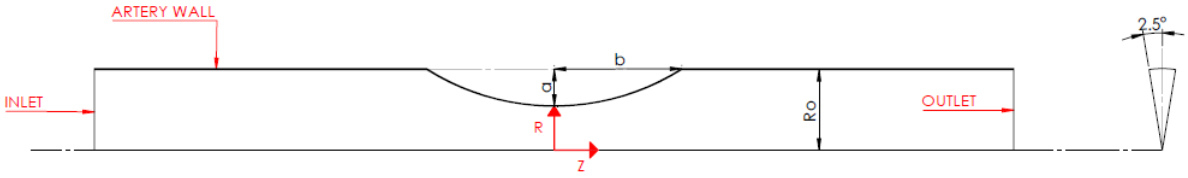

Figure 4.1: Wedge Geometry Domain

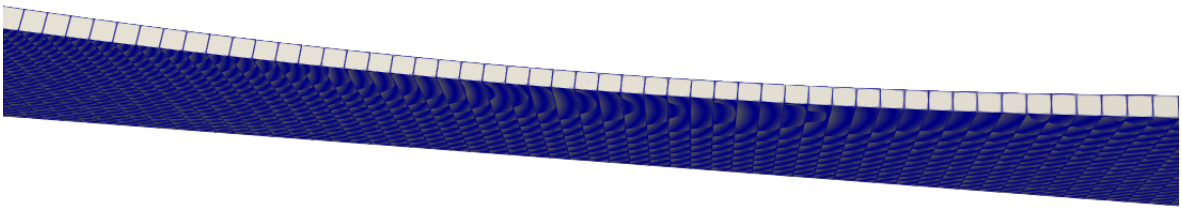

Figure 4.2: One Cell Wedge Thickness

The space discretization was done using the *blockMesh* utility in *OpenFOAM*. For the stenosis part of the geometry ($-b \leq z \leq +b$), a mesh resolution of 240x60 was chosen. 240 cells in the axial direction and 60 cells in the radial direction. The first neighbouring cells to the stenosis were created in such a way that they are the same dimensions as the stenosis cells. The rest of the cells are created in relation to those neighbouring cells with the expansion factor of 1.01 in both radial and axial direction. As a result, the total number of mesh cells is 47880 for $M1$ and $M2$ configuration and 63960 for the $M0$ configuration. From figure 4.3, it is noticeable that the mesh is finer around the stenosis arch. This allows for precise monitoring of changes in physical properties.

Figure 4.3: Generated mesh section for M2 configuration

Table 4.2: Boundary conditions

	Inlet	Outlet	Wall
Pressure (p)	zeroGradient	fixedValue	zeroGradient
Velocity (V)	fixedValue	zeroGradient	noSlip
Wall shear stress (τ)	fixedValue	zeroGradient	zeroGradient

4.2. Boundary conditions

Proper boundary condition choice is of great importance for simulation success. If they are chosen inappropriately, the simulation results will not resemble the problem in the physical world. In some cases, it will lead to solver failure. Artery wall is defined as a *wall* patch, meaning there is no fluid flow through the artery wall. Inlet and outlet are defined as patches. It is necessary to set a velocity, pressure and wall shear stress boundary conditions. As shown in Table 4.2., pressure at the inlet patch and artery wall is defined with *zeroGradient* boundary condition. The patch pressure value is obtained by extrapolating it from the nearest cell value. This means that the pressure is developed in space and its gradient is equal to zero in direction perpendicular to the patch or wall. The same boundary condition is defined for velocity at the outlet patch and for wall shear stress at the outlet and wall patch. By employing the *fixedValue* boundary condition at certain patches, the value of the physical property is kept constant. Thus, the pressure at the outlet patch is kept constant at $p_{out} = 0$. Velocity at the inlet patch is kept constant as the uniform average velocity $U_{i,avg}$ for steady state cases. Wall shear stress value at the inlet patch is also kept constant at $\tau_{in} = 0$. Velocity at the artery wall is defined with *noSlip* boundary condition. This means that the fluid velocity at the wall

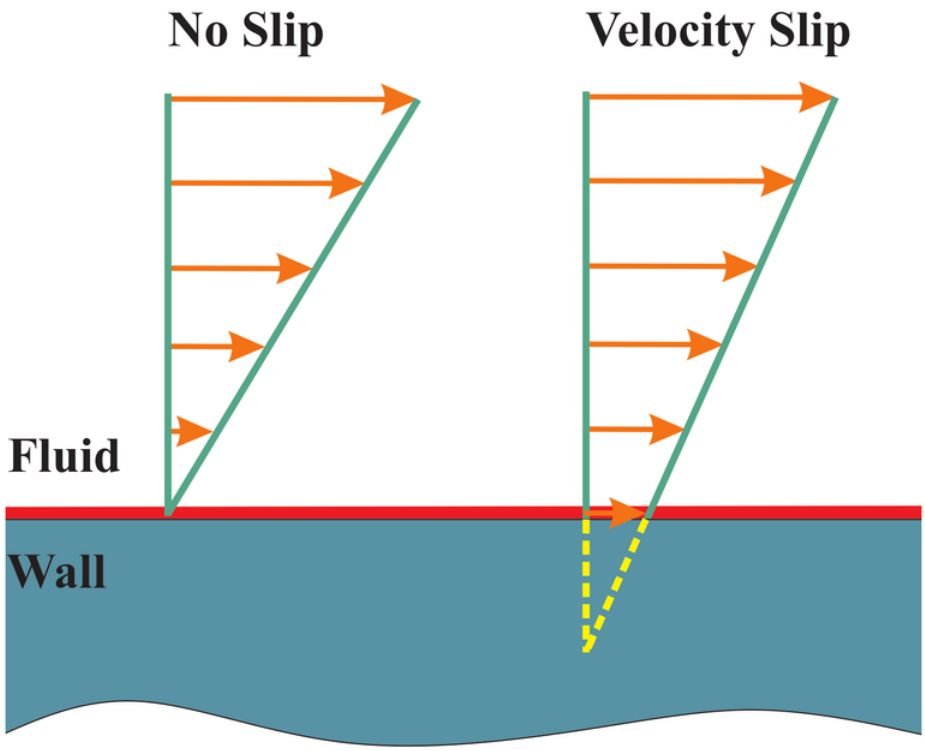

Figure 4.4: No Slip Boundary Condition [26]

is equal to the wall velocity and there is no relative movement between the fluid and the wall. If the wall is stationary, then the total velocity at the wall is equal to 0 (see Figure 4.4). If the wall is moving with a certain velocity, flow at the wall is also moving with that same velocity.

To model the pulsatile flow of blood, velocity at the inlet is defined as a sine function dependent on time t:

$$U_i(t) = U_{avg} + A\sin(\omega t) \tag{4.5}$$

where A is the amplitude and ω is the frequency. Values of the amplitude are described with a dimensionless number ϕ called the *unsteady ratio*.

$$\phi = \frac{A}{U_{i,avg}} \tag{4.6}$$

It is kept constant as $\phi = 1$, meaning that the amplitude of the velocity is at all times equal to the magnitude of the average uniform velocity at the inlet patch. Another dimensionless number, often used in hemodynamics, is introduced to describe the velocity

frequency, the Womersley number Wo.

$$Wo = R\sqrt{\left(\frac{\omega}{\nu}\right)} \tag{4.7}$$

where $\nu = \frac{\mu}{\rho}$ is the kinematic viscosity. In this study, the value of is constant and set at $Wo = 10$. Lastly, as mentioned before, the axisymmetric boundary condition is set at the z-axis of the wedge. Values of unsteady ratio ϕ and Womersley Wo are taken from Chauchan & Sasmal. [7]

5 Results

All 3 models, Newtonian, generalized Newtonian (Carreau-Yasuda) and viscoelastic (sPTT) are used to simulate flow at both $Re = 50$ and 200 and through 3 different stenosis configuration (M0, M1 and M2). Tracked values are:

- axial velocity profile at $z = 0$
- radial velocity profile at $z = 0$
- dimensionless pressure drop along the artery axis

$$\Delta\bar{p} = \frac{p_1 - p_2}{\frac{1}{2}\rho U_{avg}^2} \tag{5.1}$$

- dimensionless pressure drop difference before and after the stenosis at a distance of $\pm 16R$ from the stenosis peak

$$\Delta\bar{p} = \frac{p|_{z=-16R} - p|_{z=+16R}}{\frac{1}{2}\rho U_{avg}^2} \tag{5.2}$$

- dimensionless forces acting on the stenosis wall

$$\bar{F} = \frac{F}{\frac{1}{2}R^2\pi\rho U_{avg}^2} \tag{5.3}$$

Results are presented and discussed in the following chapters.

5.1. Comparison with literature

In this chapter, the results of this study are compared to the results from Chauchan & Sasmal [7] as a means of ensuring the validity of the models used. In that paper, the viscoelastic sPTT model and the Newtonian model is used. Therefore, comparison is done for results obtained from the sPTT and the Newtonian model used in this study. In figure 5.1, a comparison of the axial and radial velocity profiles for $M2$ configuration and steady flow is shown. Axial velocity profiles correspond almost identically. Radial velocity profiles are also in good agreement. Differences are more noticeable for the results of the viscoelastic model at $Re = 200$. In figure 5.2, a comparison of the non-dimensional pressure along the artery axis for $M2$ configuration and steady flow is presented. Results are in excellent agreement besides the prediction of viscoelastic models for $Re = 50$ before the stenosis. In the work of Chanuchan & Sasmal [7], slightly lower values are predicted.

Comparison is also done for the results of the pulsatile flow simulations. Figures 5.3 and 5.4 show the comparison of the axial velocity profiles for $M1$ configuration at $Re = 200$ for the Newtonian and viscoelastic model, respectively. The comparison for the Newtonian model shows that the results from both studies are virtually identical. However, the comparison for the viscoelastic model shows a disagreement between the results. In this study, the velocity magnitude is found to be greater than in Chauchan & Sasmal [7]. The differences are present throughout the whole cycle. Furthermore, a bit finer mesh is used in this study. No information about the time step or the CFL number that is used is presented in Chauchan & Sasmal [7]. Different time steps can also lead to variation in results. Furthermore, all the discretization schemes are also different.

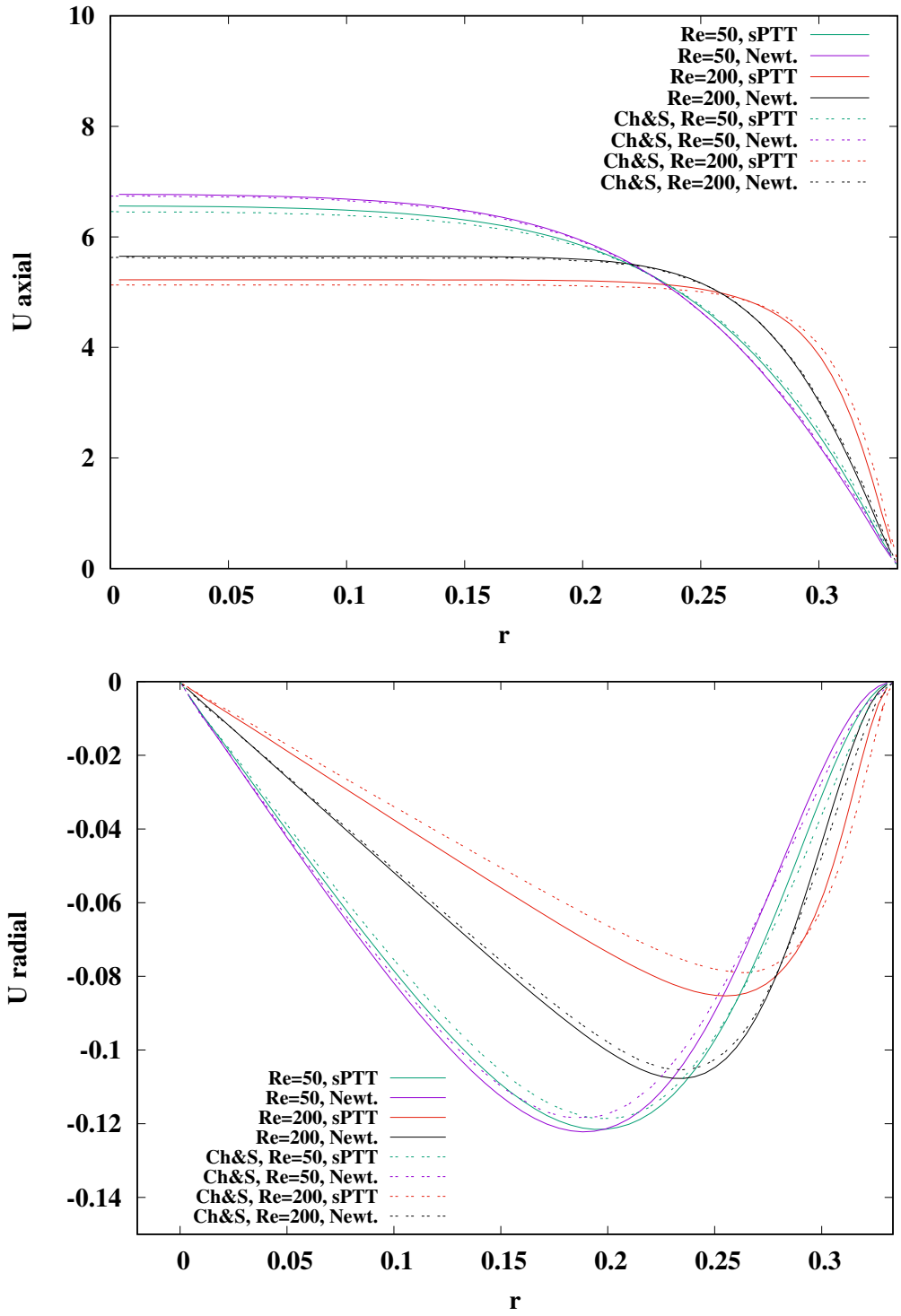

Figure 5.1: Axial and radial velocity profiles for $M2$ configuration comparison

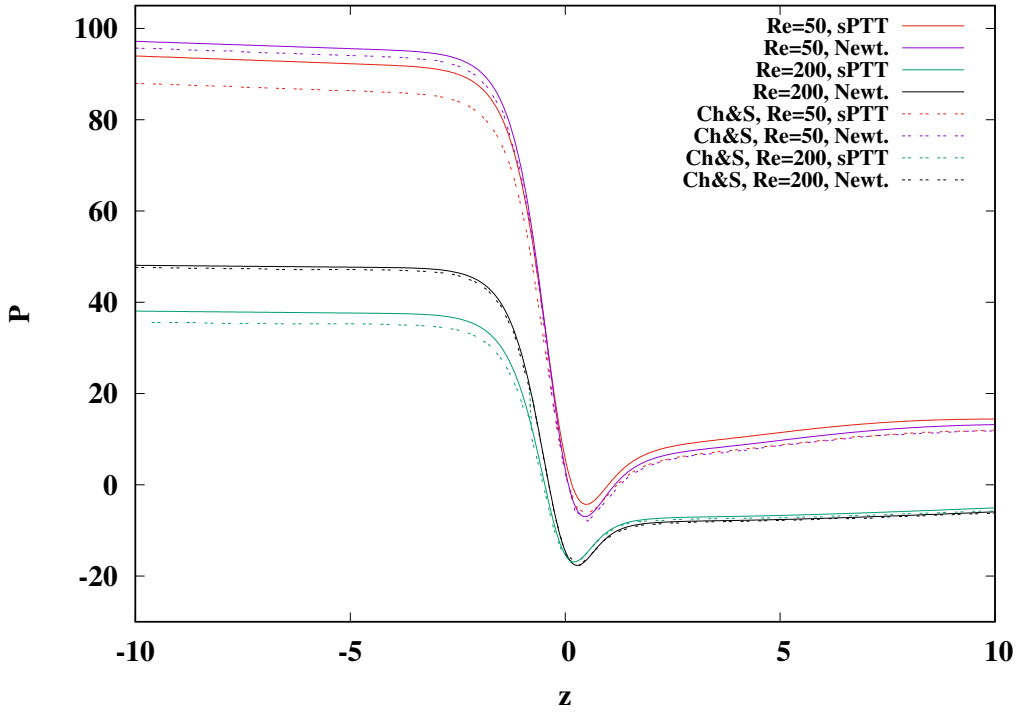

Figure 5.2: Non-dimensional pressure along the axis for $M2$ configuration comparison

5.2. Steady flow

In this chapter, the results for steady flow simulations are presented. Figures 5.5 and 5.6 show the computed streamlines of the blood flow at different Reynolds numbers. Streamlines are lines which describe the path of an imaginary particle suspended in the fluid and carried along with the flow. They are tangent to the flow velocity. This makes them useful for flow visualization. At $Re = 50$, all models exhibit almost the same velocity distribution. The velocity magnitude is increased as the flow enters the stenosis, which is expected at a reduced cross-sectional area. A boundary layer separation occurs as the flow passes the stenosis peak (past $z = 0$). Flow can not follow the stenosis shape anymore and separates. As a result, vortex, or in other words, a recirculation region is formed. Drag force is induced as a result of pressure difference upstream

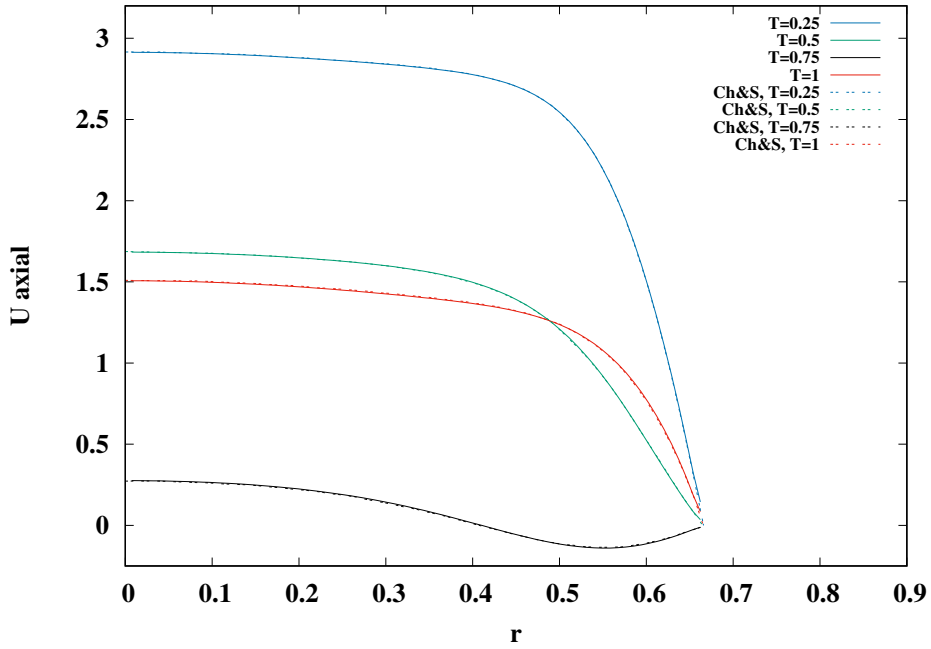

Figure 5.3: Pulsatile axial velocity profiles for $M1$ configuration at $Re = 200$ comparison (Newtonian)

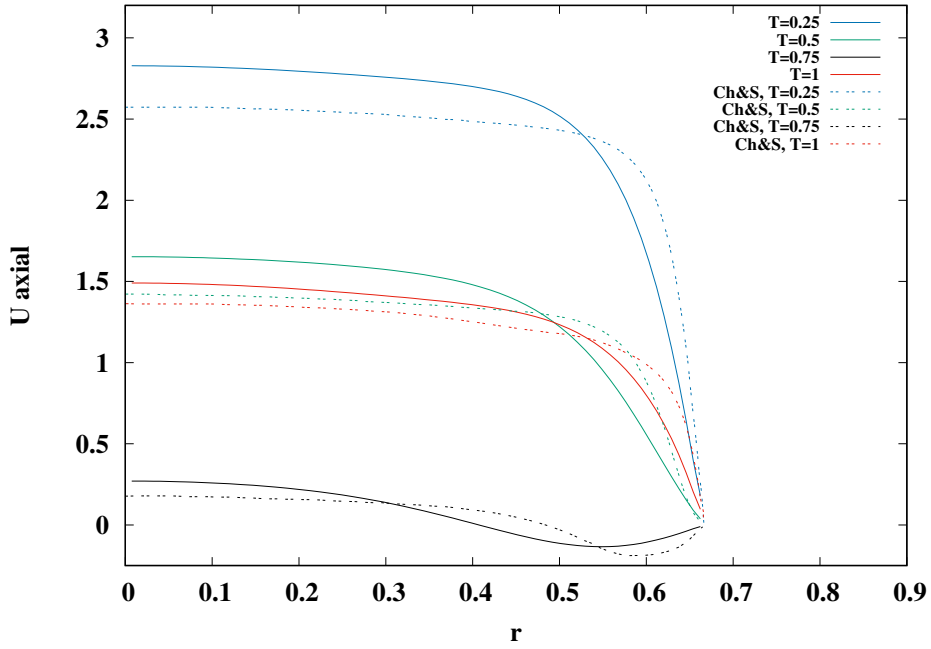

Figure 5.4: Pulsatile axial velocity profiles for $M1$ configuration at $Re = 200$ comparison (viscoelastic)

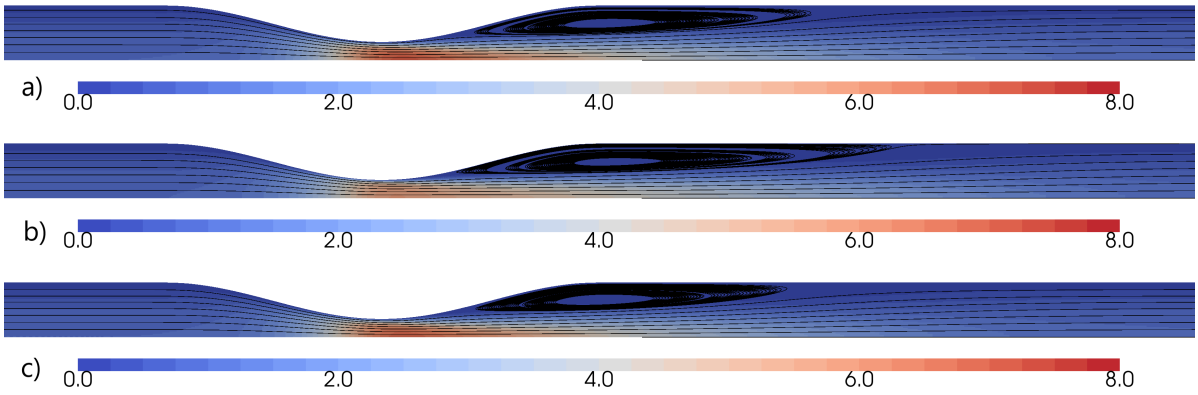

Figure 5.5: Streamlines and velocity magnitude for M2 configuration at $Re = 50$ for a) Newtonian b) generalized Newtonian and c) viscoelastic model

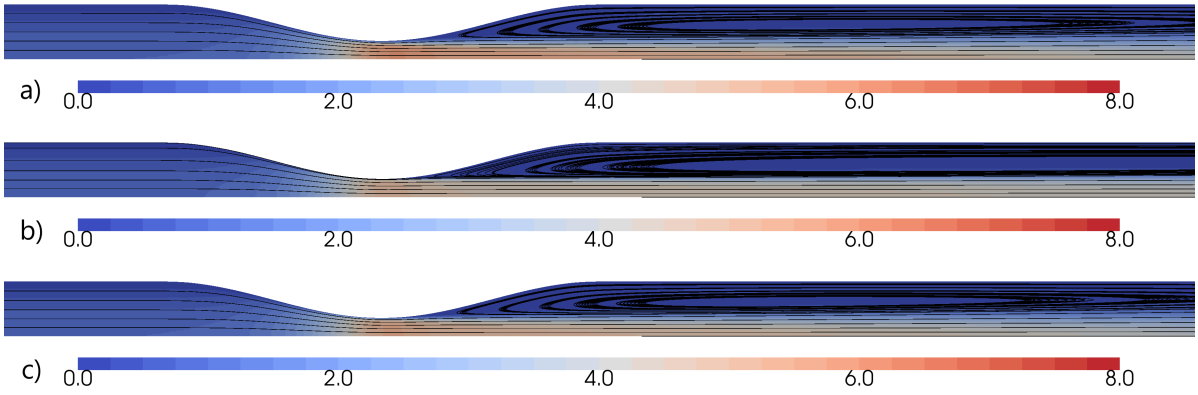

Figure 5.6: Streamlines and velocity magnitude for M2 configuration at $Re = 200$ for a) Newtonian b) generalized Newtonian and c) viscoelastic model

and downstream of the stenosis. This phenomenon is undesirable as it increases the likelihood of plaque rupture. Vortex formed in Generalized Newtonian model is longer than those of Newtonian and viscoelastic model. As the Reynolds number increases to $Re = 200$, size of the recirculation region is also increased. For the Newtonian and viscoelastic model, vortex is of almost identical shape. However, for the generalized

Newtonian model, the vortex is increased in length compared to the other two models. It can be concluded that the flow becomes more irregular at higher Reynolds numbers. For all models, stenosis peak is again the area of the greatest velocity magnitude.

In figure 5.7, a variation of the non-dimensional axial and radial velocity due to Reynolds number change and rheology model applied for M2 stenosis configuration is presented. At $Re = 50$, both axial and radial velocity profiles for the Newtonian and viscoelastic model are closely resembling each other. However, the generalized Newtonian profile deviates from the other two models. It shows lesser velocity magnitude in the middle of the artery and steeper gradient as the stenosis peak is approached. Velocity gradient near the artery wall is inversely proportional to the thickness of the boundary layer. Greater the boundary layer, lesser velocity gradient is present. Generalized Newtonian model predicts the lowest boundary layer thickness. As the Reynolds number is increased to $Re = 200$, axial velocity magnitude at the artery axis is decreased, while the gradient near the stenosis wall is increased for all three models. The velocity profile predictions of the Newtonian and viscoelastic model deviate, unlike at lesser Reynolds number. The viscoelastic model exhibits a steeper gradient and lesser velocity magnitude than the Newtonian model, while the generalized Newtonian model exhibits the steepest gradient and the lowest velocity magnitude of all three models. Higher shear-rates are present in the boundary layer. As a result, the fluid is subjected to shear-thinning and viscosity decrease when modelled as viscoelastic and as generalized Newtonian. Consequently, axial velocity magnitude is increased near the wall and decreased at the artery axis. Radial velocity magnitude is zero at the stenosis axis and wall. Negative values are a consequence of cross-sectional area reduction. At $Re = 50$, the maximum of radial velocity is found in between the stenosis axis and wall for the Newtonian and viscoelastic model, while for the generalized Newtonian that maximum is found closer to the stenosis wall. At $Re = 200$, in the same way as for axial velocity, radial velocity magnitudes are decreased for all three models. The maximums are moved closer to the artery wall. In figure 5.8, a variation of the non-dimensional axial and radial velocity at $Re = 200$ for different models and stenosis configuration is presented. The magnitudes of axial velocity are proportional to the area reduction, which is to be expected due to mass conservation principle. The steepest gradients are again predicted by the generalized Newtonian model, while the least steep gradients are predicted by the Newtonian model for all stenosis configurations. It is important to notice that the

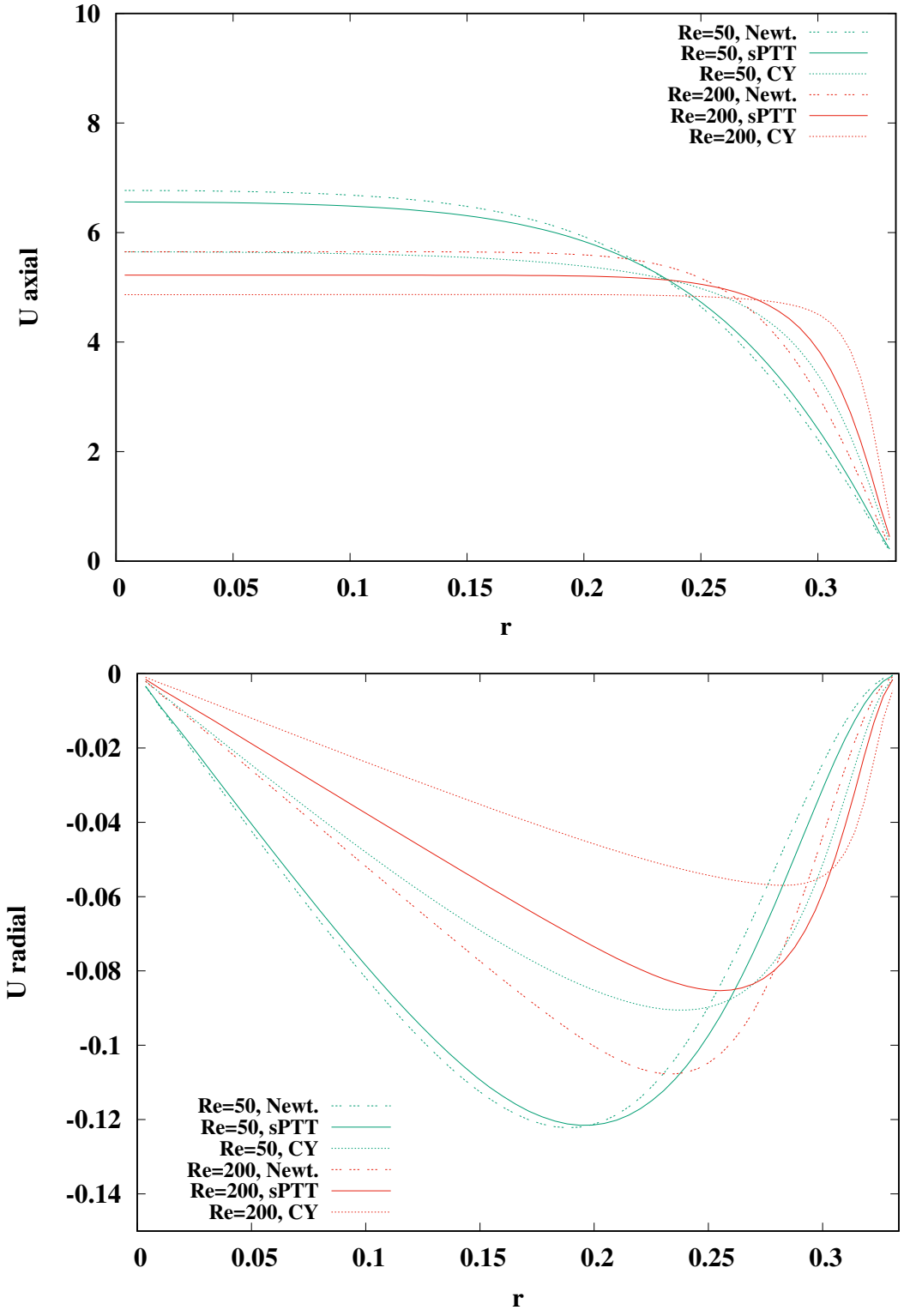

Figure 5.7: Non-dimensional axial and radial velocity variation for M2 configuration at different Reynolds numbers and models

differences between models prediction vary due to area reduction. The greater the area reduction, so are the prediction differences. For example, Newtonian and viscoelastic model predictions are virtually the same for M1 geometry, which represents the least severe stenosis. The generalized Newtonian predictions differ slightly from the other two models for M1 geometry.

In figure 5.9, the non-dimensional pressure variation at different Reynolds numbers for different models along the artery axis ($r = 0$) for $M2$ stenosis configuration is shown. All lines show the same pattern. The pressure is relatively stable up until the flow reaches stenosis. As the velocity increases due to reduction in cross-sectional area, the pressure substantially decreases. As the flow is exiting the stenosis, the pressure is increasing due to velocity reduction. Past the stenosis, pressure is beginning to stabilize again, but at a significantly lower value than before due to the pressure drop caused by the stenosis. At $Re = 50$, the generalized Newtonian model is again the one model that differs noticeably from others. It predicts lower values of pressure before the stenosis. At $Re = 200$, the difference is noticeable for all models before the stenosis with the lowest pressure value predicted by generalized Newtonian model. As the flow enters and exits the stenosis, the differences are greatly decreased. Lesser values of pressure are predicted at higher Reynolds number, since the velocity is greater. In figure 5.10, the non-dimensional pressure drop variation before ($z_1 = -16R_0$) and after ($z_2 = +16R_0$) the stenosis for all 3 models in relation to Reynolds number is shown. Since in this study, simulations are done only for $Re = 50$ and $Re = 200$, the values of pressure drop in between are approximated with a straight line. For the $M1$ configuration, which represents the least amount of area reduction, the pressure drop is also lowest as expected. The pressure drop shows substantial dependence on the Reynolds number. For the $M0$ configuration, the pressure drop is increased and Reynolds number dependency is lesser than for $M1$. For the $M2$ configuration, the prediction from the viscoelastic model shows that pressure drop is affected by the Reynolds number increase more than for other models. The generalized Newtonian model predicts the lowest amount of pressure drop overall and is almost independent of the Reynolds number increase for the $M2$ configuration. In figure 5.11, the variation of non-dimensional forces acting on the artery wall in relation to Reynolds number is shown. Again, for Reynolds number values in between $Re = 50$ and $Re = 200$, forces are approximated by a straight line. As expected, force magnitude is the greatest for the $M2$ configuration. For the $M1$ and $M0$ configuration, both

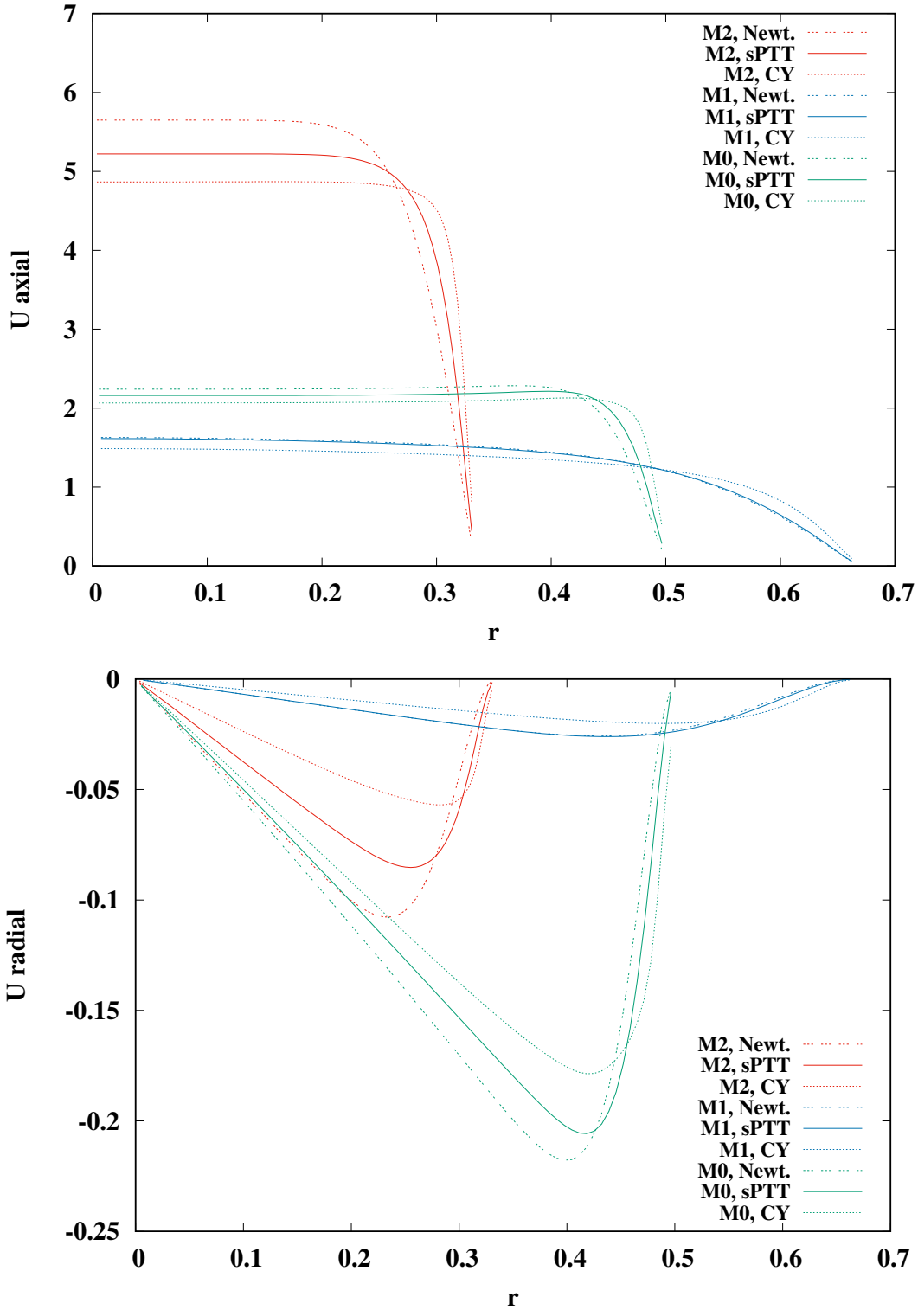

Figure 5.8: Non-dimensional axial and radial velocity variation at $Re = 200$ for different models and stenosis configuration

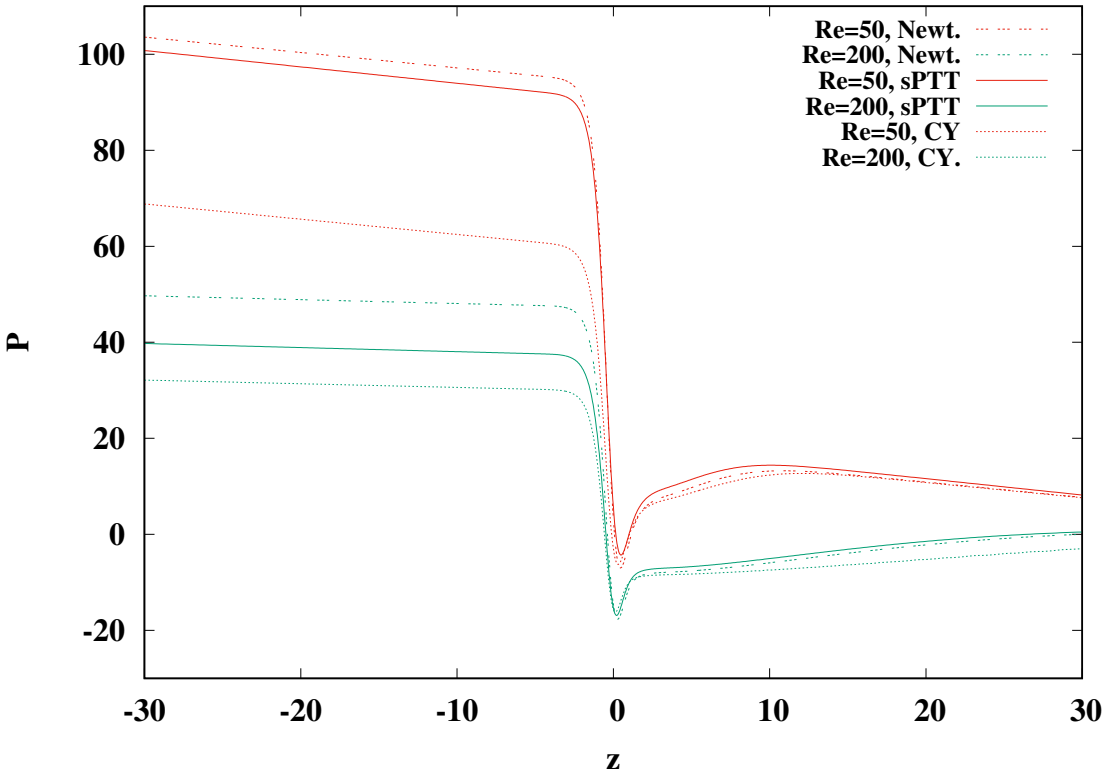

Figure 5.9: Non-dimensional pressure variation along the artery axis ($r = 0$) for $M2$ stenosis configuration

magnitude and Reynolds number dependency predictions of the forces are very similar for all models. As the Reynolds number is increased, the force magnitude is decreased. Generalized Newtonian model predicts the lowest amount of forces acting on the artery wall. That difference is substantial for the $M2$ configuration. It can be concluded that the appropriate model choice is more important when the stenosis is more severe.

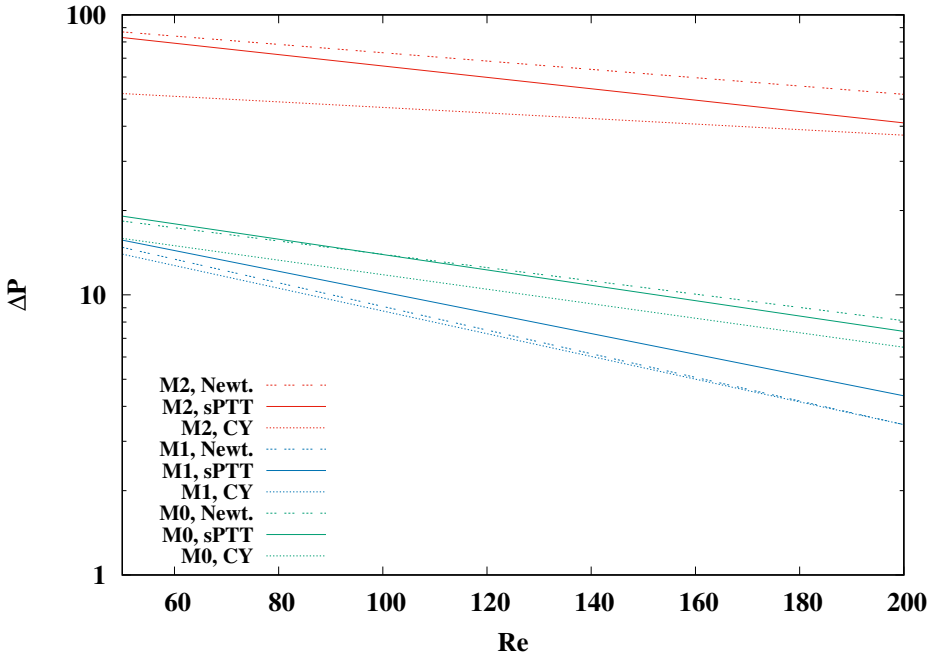

Figure 5.10: Non-dimensional pressure drop variation before ($z_1 = -16R_0$) and after ($z_2 = +16R_0$) the stenosis

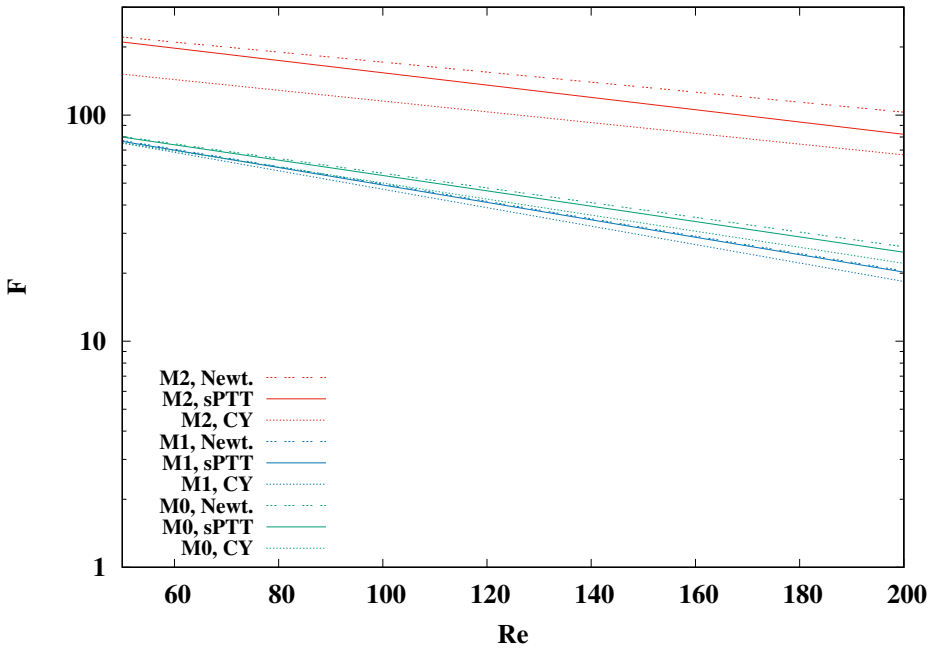

Figure 5.11: Non-dimensional forces acting on artery wall variation in relation to Reynolds number

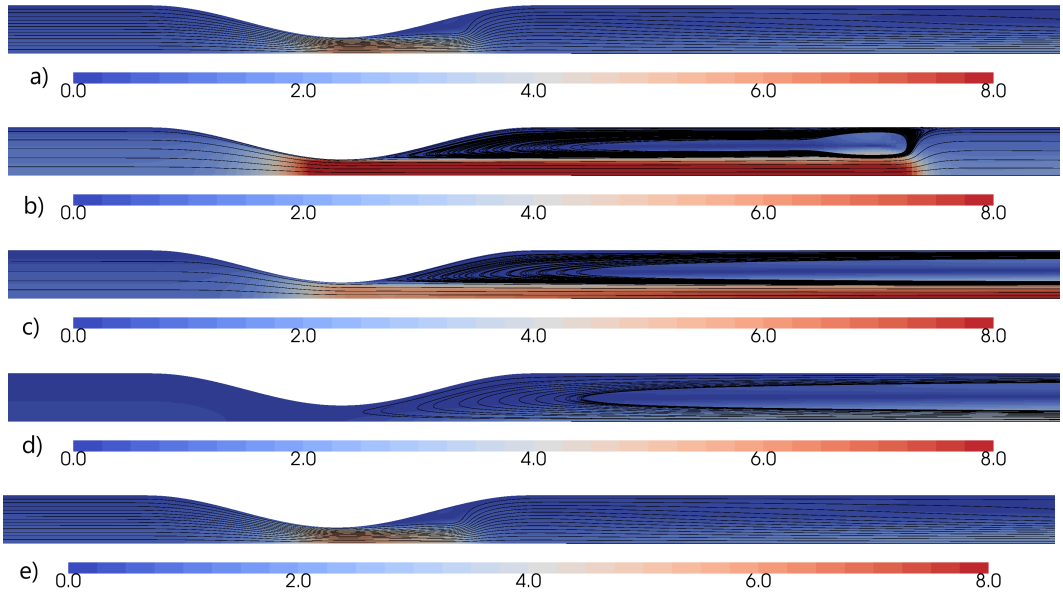

Figure 5.12: Streamlines and velocity magnitude of Newtonian model for M2 configuration at $Re = 200$ a) $T = 0$ b) $T = 0.25$ c) $T = 0.5$ d) $T = 0.75$ e) $T = 1$

5.3. Pulsatile flow

In this chapter, the results for pulsatile flow simulations are presented. In figures 5.12, 5.13 and 5.14 the streamlines and velocity magnitudes of a single repeating cycle for the M2 configuration at $Re = 200$ for Newtonian, generalized Newtonian and viscoelastic model are presented, respectively. Time passed during one periodic cycle is denoted with T ranging from 0 as the cycle beginning to 1 as the cycle end. At $T = 0$, the heart begins to contract and pump blood. Streamlines are mostly attached to the artery wall, with minor boundary separation after the stenosis peak. At $T = 0.25$, velocity magnitude is at its maximum. Vortices are formed as the streamlines separate from the wall. At $T = 0.5$, the vortices are still present but their length is increased. At $T = 0.75$, the flow velocity is greatly reduced compared to the maximum. At $T = 1$, flow returns to initial state and the cycle is repeated. Generalized Newtonian model predicts the highest amount of flow irregularities compared to other models, while the Newtonian models predicts the lowest amount.

In figure 5.15, a variation of the axial velocity over one periodic cycle for $M1$

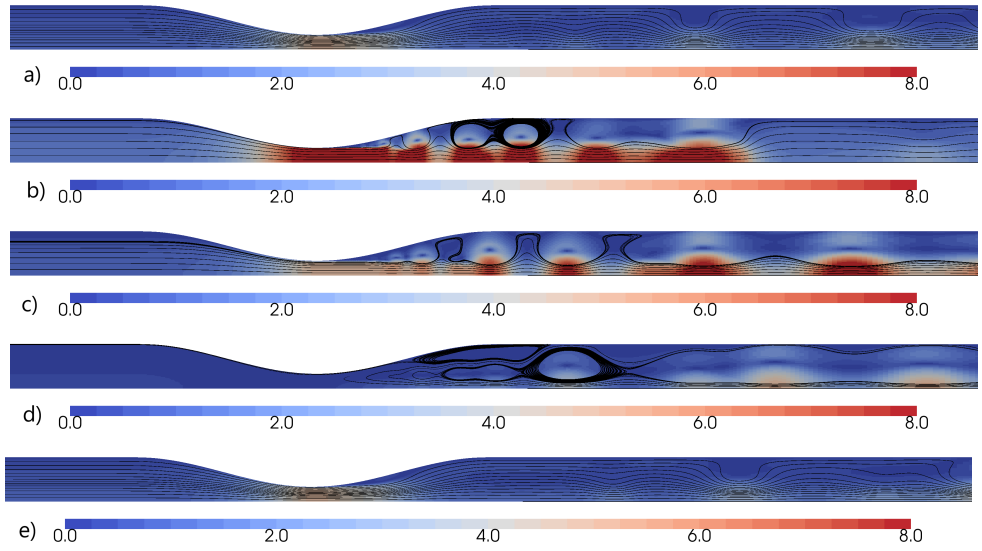

Figure 5.13: Streamlines and velocity magnitude of generalized Newtonian model for M2 configuration at $Re = 200$ a) $T = 0$ b) $T = 0.25$ c) $T = 0.5$ d) $T = 0.75$ e) $T = 1$

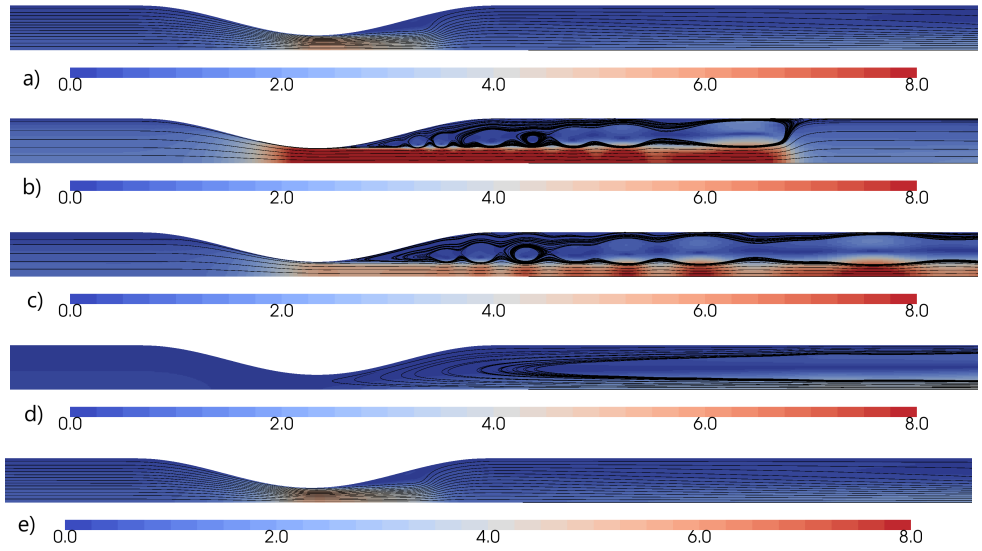

Figure 5.14: Streamlines and velocity magnitude of viscoelastic model for M2 configuration at $Re = 200$ a) $T = 0$ b) $T = 0.25$ c) $T = 0.5$ d) $T = 0.75$ e) $T = 1$

configuration at $Re = 200$ is presented. In agreement with the steady flow results, the generalized Newtonian model predicts the lowest velocity magnitude at the artery axis and the steepest gradient near the stenosis wall. This discrepancy is present during the whole cycle and is more noticeable as the velocity magnitude increases. The Newtonian and viscoelastic model predictions are in excellent agreement even at higher velocities, while being almost indistinguishable at the cycle beginning and end. In figure 5.16, non-dimensional pressure drop variation before ($z_1 = -16R_0$) and after ($z_2 = +16R_0$) the stenosis over one cycle at $Re = 200$ for three stenosis configurations is shown. All three models are in agreement for all configurations, especially $M0$ and $M1$. For $M2$ configuration, as is shown in the streamlines figures, the vortices are formed as the velocity starts to decrease from its maximum at $T = 0.25$. Those vortices explain the spikes that occur in the pressure drop lines. For the Newtonian model, the vortices cease to exist quickly, while for the generalized Newtonian model they can be seen

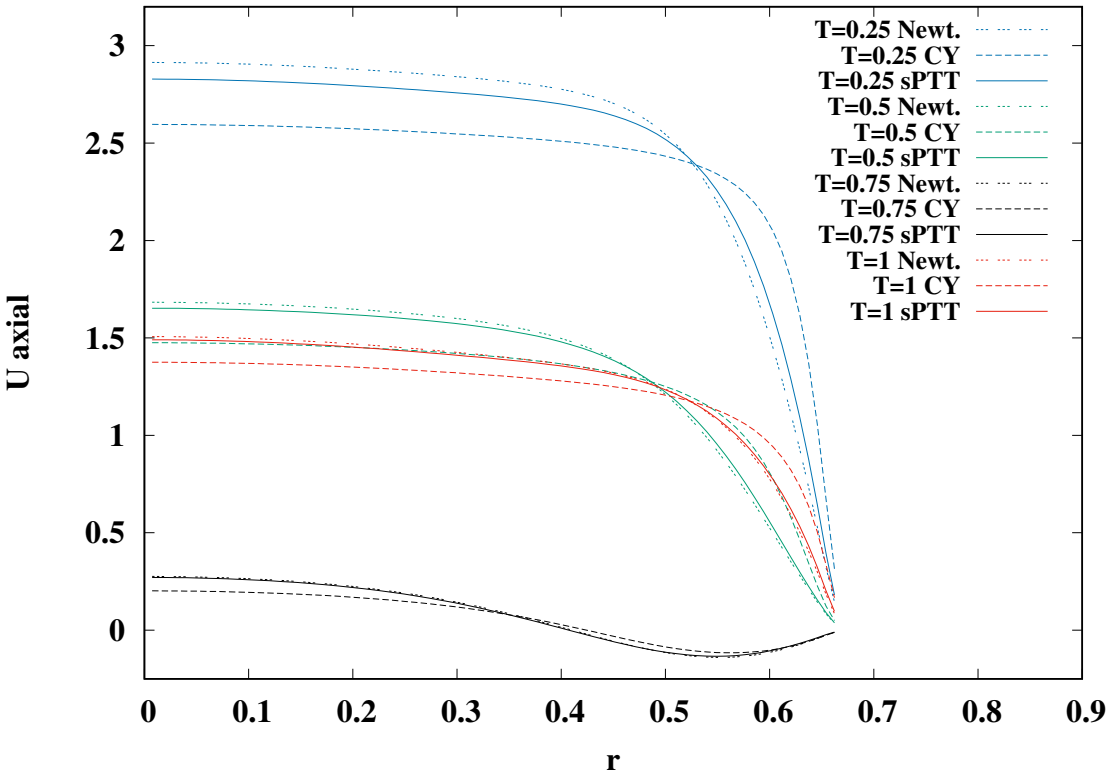

Figure 5.15: Axial velocity variation over one cycle for $M1$ configuration at $Re = 200$

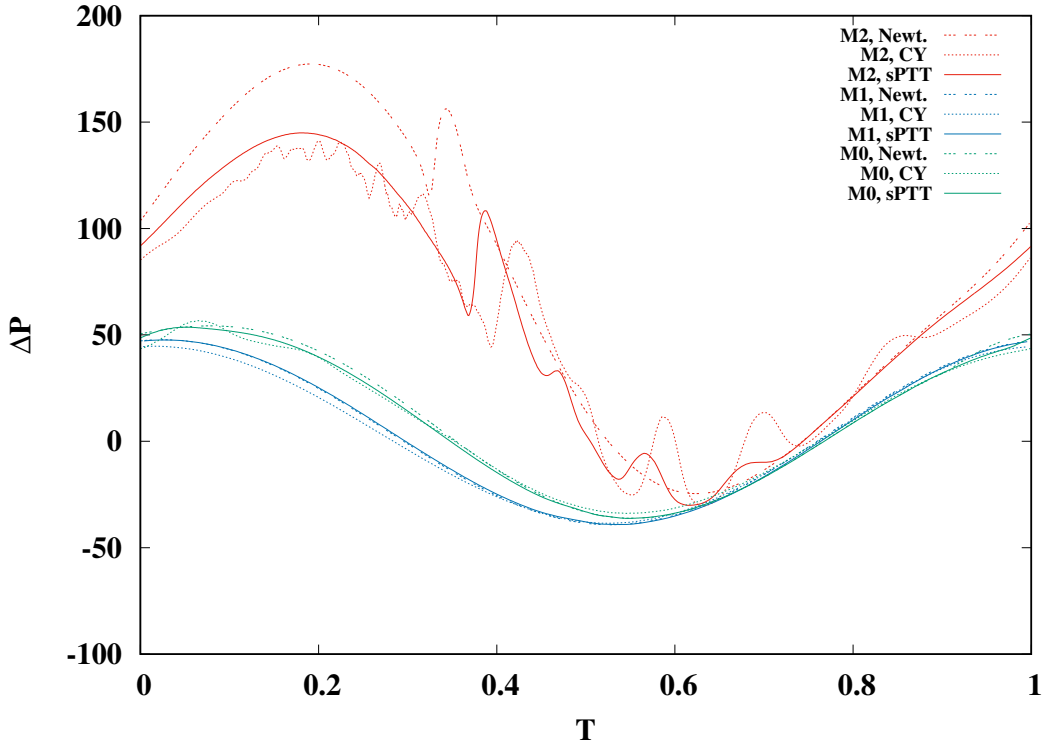

Figure 5.16: Non-dimensional pressure drop variation before ($z_1 = -16R_0$) and after ($z_2 = +16R_0$) the stenosis over one cycle at $Re = 200$ for three stenosis configurations

even at $T = 0.75$. For $M0$ and $M1$ configurations, the vortices and irregularities are present in a much smaller degree. Pressure drop is at its maximum at around $T = 0.2$, while the minimum is found around $T = 0.5$. For $M2$ configuration, the maximum and minimum values are found a bit later in the cycle than for other configurations. In figure 5.17, the non-dimensional forces acting on artery wall variation over one cycle at $Re = 200$ for three stenosis configurations is presented. Similar to pressure drop variation, the maximum is found at around $T = 0.2$, while the minimum is found around $T = 0.65$. The Newtonian and viscoelastic models are in good agreement, except for the $M2$ configuration. As expected from previous conclusions, the generalized Newtonian model predicts the lowest magnitude of force for all configurations. These results confirm the conclusion from the steady flow results. It can be stated that the model prediction differences are greater as the severity of the stenosis and the velocity magnitude is greater.

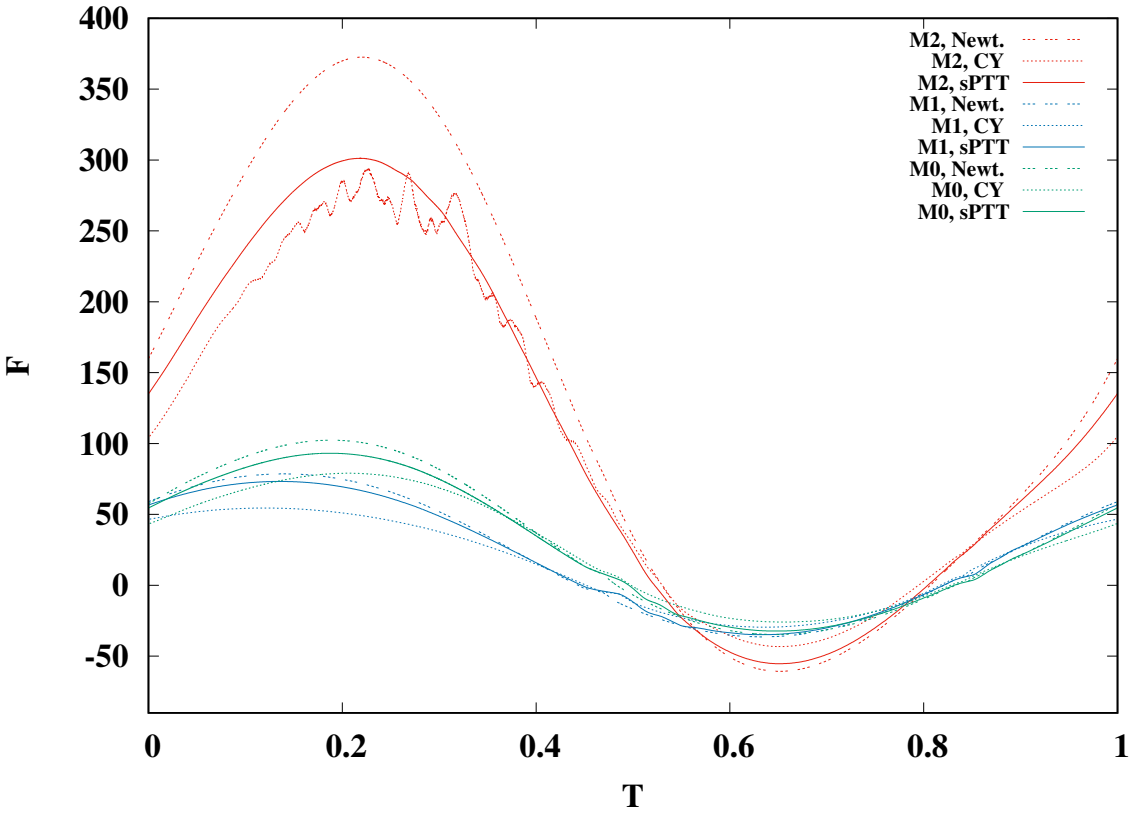

Figure 5.17: Non-dimensional forces acting on artery wall variation over one cycle at $Re = 200$ for three stenosis configurations

6 Conclusion

Coronary artery disease is one of the leading causes of death globally. Identifying and assessing the risk of formed plaque rupture is of vital importance. One of the ways to study coronary artery disease is using computational fluid dynamics (CFD). In order for the CFD results to resemble reality, an appropriate rheology model for blood must be chosen, among many other things. Blood rheology is a complex issue and its flow properties depend on various factors.

In this study, the effects of three different rheological models of blood on the flow through an idealised stenosed artery are studied. It is assumed that the arterial wall is rigid and that the flow is isothermal, while blood is modelled as an incompressible fluid with three rheological models: Newtonian; generalized Newtonian, with the Carreau-Yasuda model; and viscoelastic, with the simplified Phan-Thien-Tanner model. The impact of stenosis shape is also studied by considering three geometries with varying length and height at two Reynolds numbers: Re=50 and Re=200. Both steady state and pulsatile flow are simulated, hence 36 simulations were run in total. Results show that the Carreau-Yasuda model predicts noticeably lesser magnitudes of velocity at the artery axis than the other two models. The boundary layer size is the smallest for the Carreau-Yasuda model resulting in the steepest velocity gradient near the artery wall. The pressure and resulting forces magnitudes are also the smallest for the Carreau-Yasuda model. The differences between model predictions become more pronounced, as Reynolds number and stenosis severity increase. The resulting forces acting on the artery wall are greater as the cross-sectional area is more reduced.

This study was greatly influenced by the work of Chauchan & Sasmal [7], hence their

results were used to validate the results of the present study. An excellent agreement is found between the results except for the velocity profiles for pulsatile flow predicted by the sPTT model. These deviations likely result from differences in discretization schemes and temporal resoultion.

Hopefully, this study will serve as a basis for future studies related to hemodynamics. In future works, the fluid-solid interaction between blood and atherosclerotic plaques should be investigated. This would provide a more detailed insight into how plaques are affected by the blood flow and likely help in identification of those plaques which are most likely to rupture. If they are identified, precautionary measures can be taken to prevent fatal results.

Bibliography

[1] Cardiovascular system. https://www.thoughtco.com/cardiovascular-system-373577.

[2] How does blood flow through your body ? https://my.clevelandclinic.org/health/articles/17059-how-does-blood-flow-through-your-body.

[3] M. Krajcar. Rekonstrukcija geometrije koronarne arterije iz CT snimke. *Faculty of Mechanical Engineering and Naval Architecture*, 2021.

[4] Heart. https://www.britannica.com/science/heart.

[5] C. T. Dotter, D. J. Roberts, and I. Steinberg. Aortic length: angiocardiographic measurements. *AHA Journals*, 2(6):915–920, 1950.

[6] What's the difference between arteries, veins, and capillaries? https://www.webmd.com/heart/difference-between-arteries-veins-capillaries.

[7] A. Chauhan and C. Sasmal. Effect of real and whole blood rheology on flow through an axisymmetric stenosed artery. *International Journal of Engineering Science*, 169:103565, 2021.

[8] Coronary artery disease. https://www.rwjbh.org/treatment-care/heart-and-vascular-care/diseases-conditions/coronary-artery-disease/.

[9] Lipids and Lipoproteins in Atherosclerosis. https://www.ncbi.nlm.nih.gov/pmc/articles/PMC3317094/.

[10] A. Gholipour, M. H. Ghayesh, A. Zander, and R. Mahajan. Three-dimensional biomechanics of coronary arteries. *International Journal of Engineering Science*, 130:93–114, 2018.

[11] The relationship between blood pressure and blood viscosity. https://www.meridianvalleylab.com/the-relationship-between-blood-pressure-and-blood-viscosity/.

[12] Newton's law of viscosity. https://mechcontent.com/newtons-law-of-viscosity/.

[13] G.B. Thurston. Viscoelasticity of Human Blood. *Biophysical Journal*, 12(9):1205–1217, 1972.

[14] F. Rizzo, F. Pinto, and M. Meo. Investigation of Silica-Based Shear Thickening Fluid in Enhancing Composite Impact Resistance. *Applied Composite Materials*, 27, 06 2020.

[15] K. McGurk, B. Owen, W.D. Watson, R. Nethonoda, H. Cordell, M. Farrall, O. Rider, H. Watkins, A. Revell, and B. Keavney. Heritability of haemodynamics in the ascending aorta. *Scientific Reports*, 2020:14356, 09 2020.

[16] Turbulent flow. https://www.cvphysiology.com/Hemodynamics/H007.

[17] K. K. Yeleswarapu, M. V. Kameneva, K. R. Rajagopal, and J. F. Antaki. The flow of blood in tubes: theory and experiment. *Mechanics Research Communications*, 25(3):257–262, 1998.

[18] F. A. Morrison. Polymer Rheology (Generalized Newtonian Fluids). *Michigan Technological University*, 2018.

[19] S. E. Spagnolie A. Morozov. Complex Fluids in Biological systems. 2015.

[20] Z. Virag and I. Džijan. Računalna dinamika fluida. *Faculty of Mechanical Engineering and Naval Architecture*, 2014.

[21] H. Medina, A. Beechook, J. Saul, S. Porter, S. Aleksandrova, and S. Benjamin. Open source Computational Fluid Dynamics using OpenFOAM. 11 2015.

[22] H.G. Weller, G. Tabor, and C. Jasak, H.and Fureby. A Tensorial Approach to Computational Continuum Mechanics Using Object Orientated Techniques. *Computers in Physics*, 12:620–631, 11 1998.

[23] OpenCFD release OpenFOAM® v2012 (20 12). https://www.openfoam.com/news/main-news/openfoam-v20-12.

[24] OpenFOAM guide/the PISO algorithm in OpenFOAM. https://openfoamwiki.net/index.php/OpenFOAM_guide/The_PISO_algorithm_in_OpenFOAM.

[25] J.L. Favero, A.R. Secchi, N.S.M. Cardozo, and H. Jasak. Viscoelastic flow analysis using the software OpenFOAM and differential constitutive equations. *Journal of Non-Newtonian Fluid Mechanics*, 165(23):1625–1636, 2010.

[26] A. Klothakis, G. Lygidakis, and I. Nikolos. Numerical analysis of rarefied gas flows using the academic CFD code galatea. 06 2016.

A Appendix

1. CD-R disc